Epitaxial growth of lateral graphene / hexagonal boron nitride heterostructures

Md Nurul Huda

School of Science

Thesis submitted for examination for the degree of Master of Science in Technology.

Espoo 19.10.2016

Thesis supervisor:

Prof. Peter Liljeroth

Thesis advisor:

D.Sc. (Tech.) Robert Drost

Aalto University
School of Science

AALTO UNIVERSITY
SCHOOL OF SCIENCE

ABSTRACT OF THE
MASTER'S THESIS

Author: Md Nurul Huda

Title: Epitaxial growth of lateral graphene / hexagonal boron nitride heterostructures

Date: 19.10.2016 Language: English Number of pages: 4+42

Department of Applied Physics

Professorship: F3005 –Physics of Advanced Materials

Supervisor: Prof. Peter Liljeroth

Advisor: D.Sc. (Tech.) Robert Drost

With the growing 2D materials family, the combination of the semi-metal graphene, insulator hexagonal boron nitride (h-BN) and semiconducting transition metal dichalcogenides open new opportunities in understanding and controlling materials properties. The integration of graphene with h-BN in particular is considered as a promising way to engineer the electrical properties of graphene and implementation of more advanced theoretical ideas such as valleytronics in 2D materials. In this thesis work, lateral graphene and boron nitride heterostructures are synthesized by a sequential epitaxial growth method on nickel films and Ni(111) single crystals. The edges of the BN island act as a seed for graphene growth and atomically sharp graphene / h-BN interfaces with a length exceeding 170 nm could be achieved. This is limited by the size of h-BN seed islands. We also attempted the transfer of the heterostructures onto an insulating substrate by the electrochemical delamination method. While this method worked for transferring graphene grown on Ni foil, it was unsuccessful for the G/h-BN heterostructures. Most likely, the strong interaction between heterostructure and Ni(111) causes this failure. The interaction could be reduced by intercalating the heterostructure with different materials such as Br. Further work on the combination of the transfer techniques with our synthesis method followed by intercalation should make it possible to manufacture and transfer G/h-BN heterostructures onto insulating substrates.

Keywords: Graphene, Heterostructure, G/h-BN interface, Electrochemical bubbling transfer,

Preface

First I would like to thank my supervisor, Professor Peter Liljeroth for giving me a chance to do these experiments. Then, I also thank my advisor, Dr Robert Drost for his patience in teaching me using STM. Along with them, I thank all members of the Atomic Scale Physics group, for encouragement, support, and advice during this thesis project. I thank Kaustuv Banerjee for his support during transferring process. I also thank Dr Sanna Arpiainen (VTT) for her significant contributions to the experimental setup for the transfer process.

I also thank to my family members for their encouragement and mental support.

Otaniemi, Espoo. October 19, 2016

Md Nurul Huda

Contents

1 Introduction

The combination of different materials into heterostructures has always been a potential method for controlling material properties. There are several two dimensional (2D) materials such as graphene, hexagonal boron nitride (h-BN) and transition metal dichalcogenides with distinct electrical properties. The combination of these materials into heterostructures opens a new opportunity in manipulating their properties [1]. Recent experiments have shown great potential of the stacked 2D materials in transistor operation [2]. Additionally, the combination of covalently bonded 2D materials in the same plane can give control over electrical properties and yield devices with new unique properties [3].

While fabrication techniques of graphene-BN heterostructures with a feature size down to below 100 nm has been demonstrated, control of the interface properties down to the atomic scale is important for applications. [3] [4]. Zigzag terminated graphene nanostructures could enable spintronics in graphene [5] and passivation of such nanostructures by h-BN would allow their transfer onto different substrates while keeping the atomic structure unchanged. There are two main approaches to fabricate graphene-BN heterosturctures: pattern re-growth technique [3] and sequential epitaxial growth [6]. While the large scale growth of G/h-BN patterns is possible by pattern re-growth method, there is no atomic scale control over interface structure. A more promising approach is sequential epitaxial growth of graphene and BN on transition metals, where regular edge structures are readily obtained. In this method, the edge of the first material acts as a seed for the second material. The previous experiments have focused on the metal surfaces for graphene growth such as Ir(111) [7] [8], Rh(111) [9] , Ru(0001) [10] and Cu foils [11]. The formation of the moiré pattern of graphene and h-BN have been reported on those metal surfaces because of the lattice mismatch between graphene and metal substrate. Even though the lattice constants of graphene and h-BN are closely matched, the moiré patterns have different periods and this leads to strain induced defect formation at the interface on these surfaces [10]. On the other hand, Ni(111) is a strongly interacting crystal facet having a lattice constant closely matched with both graphene and h-BN. Both of these materials form 1×1 structures on Ni(111) because of strong interaction. The absence of moiré pattern on Ni(111) makes it an ideal surface for the controlled synthesis of extended, atomically well defined G/h-BN interfaces [6].

The graphene-BN heterostructures on Ni(111) need to be transferred onto insulating substrates for further applications and basic research. A lot of efforts has already been directed to transfer 2D materials by electrochemical etching method. In this case, the substrate is etched away during the transfer process. The etching transfer not only increases the production cost but also requires long treatment cycles of several hours. On the other hand, a transfer method by electrochemical bubbling was recently proposed by Wang et al. [12], and Gao et al [13]. This enables the facile transfer of graphene without the destruction of the catalytic metal substrate. In this work, after studying the formation of graphene, h-BN and their heterostructures on Ni(111) by STM, we demonstrate a nondestructive route to transfer G/h-BN heterostructures from the substrate by electrochemical bubbling process.

2 Theory and Experimental Background

2.1 Graphene

Graphene is two dimensional crystal of carbon atoms, forming a hexagonal honeycomb lattice with sp^2-hybridized bonds. Graphite is formed by the stacking these planes on top of each other. The abundancy of carbon materials with different properties is the result of the versatility of the C-C bonds. Graphene can be considered to be the origin of all the different nanocarbon allotropes (see the Figure 1). It is the only 2D member among the other carbon allotropes such as 0D fullerene, 1D carbon nanotube, and 3D graphite. Graphene is an interesting nano-material with extraordinary electrical and mechanical properties which makes it a candidate for a large variety of applications. For instance, it is about 100 times stronger than the strongest steel. It conducts heat efficiently, and it is an extremely good electric conductor. Because of these properties graphene is called a wonder material, and it could also potentially replace silicon as the material of choice in electronics. These unique features of graphene can be understood by analysing its structural and electrical properties.

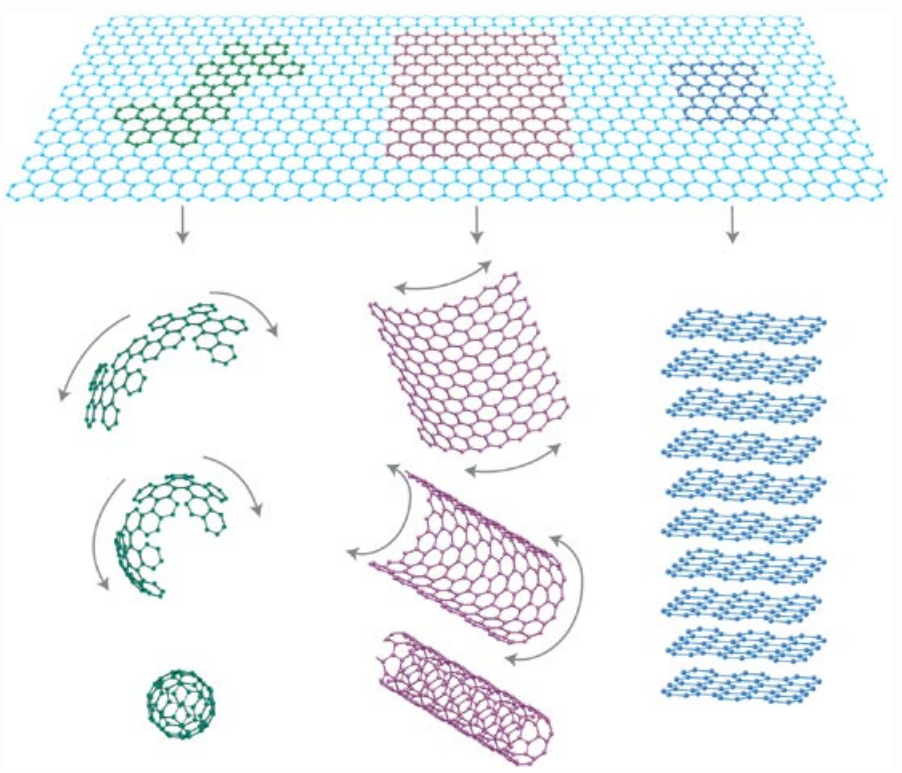

Figure 1: The allotropes of carbon materials. 2D graphene can be thought as building material of other carbon allotropes. From the left, fullerenes which is wrapped into OD buckyballs, carbon nanotube where graphene is rolled into 1D carbon nanotube and lastly graphene sheets are stacked together to form 3D graphite. Adapted from Ref [14].

2.1.1 Structure

The graphene 2D sheet is held together with strong sp^2 bonds between the carbon atoms separated by a distance of 1.4 Å which gives graphene its strong mechanical properties. To understand the electronic structure of graphene we have to discuss its honeycomb lattice. The honeycomb lattice can be analyzed as triangular lattice with a two-atom unit cell (see Figure 2). The entire lattice can be constructed by translating this cell along the lattice vectors. There are two possible high symmetry cuts along a honeycomb lattice. These are called "armchair" and "zig-zag" due to the appearance of the resulting jagged edge along such a cut (see Figure 2). The orientation of a lattice, especially the orientation of the edges along the armchair or zig-zag direction, has interesting fundamental effects on the electronic behaviour of graphene.

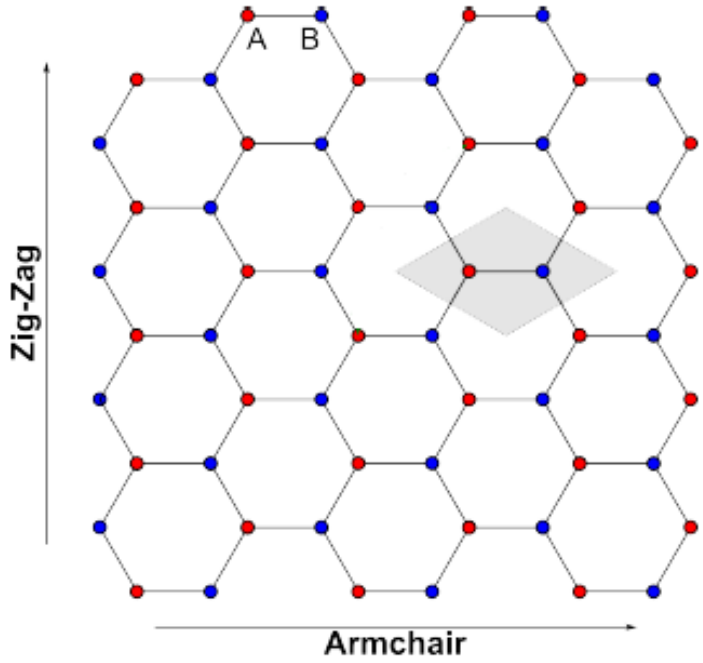

Figure 2: Structure of graphene. Light blue shadow represent a unit cell of graphene containing two carbon atoms. The A sublattice sites are marked in red and the B sublattice sites in blue. Adapted from the Ref [15].

2.1.2 Electrical Properties

The electronic structure of an isolated C atom is $1s^2 2s^2 2p^2$ where 1s electrons remain more or less inert while 2s and $2p$ orbitals hybridize. Three sp^2 hybridized orbitals are formed, leaving over an unaffected p-orbital. In this case the natural tendency of these three sp^2 orbitals to arrange themselves in a plane with 120 degree angles which leads to the honeycomb structure of graphene. These sp^2 orbitals give rise to σ bond with the neighbouring carbon atoms. The unaffected p orbitals form a half-filled π band, which plays an important role in the electronic properties of graphene.

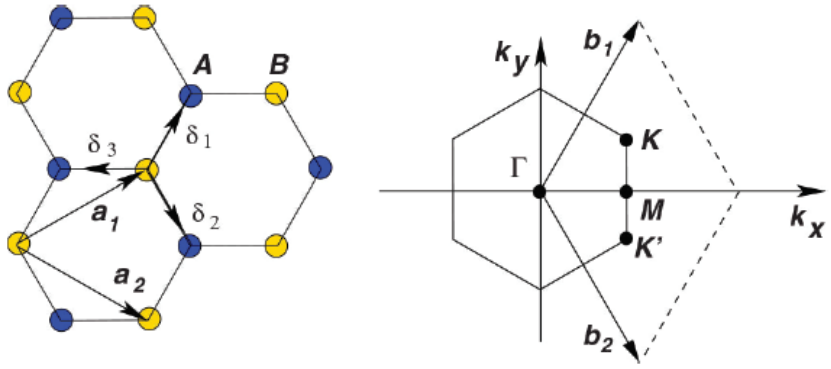

Figure 3: The honeycomb lattice of graphene and its first Brillouin zone. a_1 and a_2 are the lattice vectors and b_1 and b_2 are the corresponding reciprocal lattice vectors. Adapted with permission, Ref [16].

There are two atoms in the unit cell of graphene. According to Figure 3 the lattice vectors can be written as

$$\vec{a_1} = \frac{a}{2}(3, \sqrt{3}), \vec{a_2} = \frac{a}{2}(3, -\sqrt{3}) \tag{1}$$

where a is the nearest-neighbour C-C spacing. The reciprocal lattice vectors b_1 and b_2 are defined by the condition $a_i \cdot b_j = 2\pi\delta_{ij}$ and therefore

$$\vec{b_1} = \frac{2\pi}{3a}(1, \sqrt{3}), \vec{b_1} = \frac{2\pi}{3a}(1, -\sqrt{3}) \tag{2}$$

For the electronic properties of graphene, two points of the first Brilloiuin zone, **K** and **K'** (see Figure 3) are very important. This two points are called Dirac points, and their positions in the reciprocal space are

$$\mathbf{K} = (\frac{2\pi}{3a}, \frac{2\pi}{3\sqrt{3}a}), \mathbf{K'} = (\frac{2\pi}{3a}, -\frac{2\pi}{3\sqrt{3}a}) \tag{3}$$

The band structure of the graphene can be approximated accurately by a tight-binding model. This allows us to derive an approximate analytic formula for the conduction and valence bands

$$E_{\pm}(\mathbf{q}) \approx 3t' \pm v_F\,|\mathbf{q}| - (\frac{9t'a^2}{4} \pm \frac{3a^2}{8} sin(3\theta_{\mathbf{q}}))|\mathbf{q}|^2 \tag{4}$$

where $v_F = 3ta/2$, $\theta = arctan^{-1}(q_x/q_y)$ and t and t' are nearest neighbour($A \leftrightarrow B$) and next-nearest neighbour ($A \leftrightarrow A, B \leftrightarrow B$) hopping amplitudes. The band structure of graphene is illustrated as shown in the Figure 4. The most important feature of the band structure of graphene is the linear energy-momentum relationship with the conduction and valence bands intersecting at the K and K' points, with no energy gap. This makes graphene as zero band gap semiconductor. Another remarkable feature of the Fermi velocity of graphene v_F is the order of 10^6 ms^{-1}.

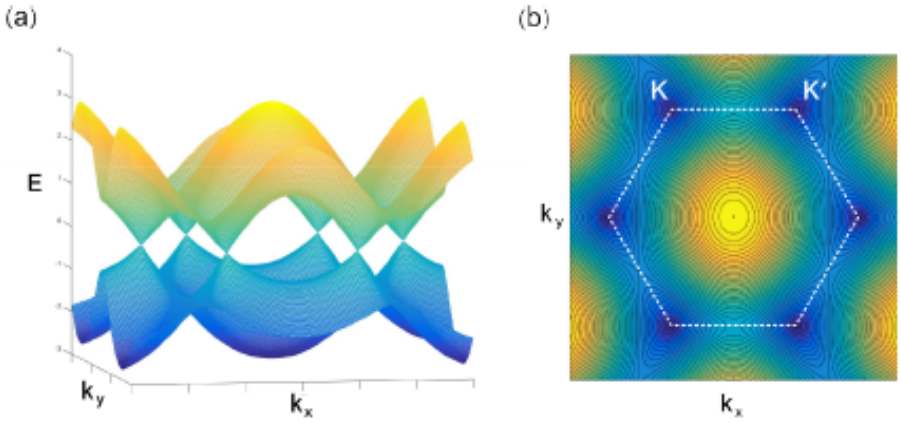

Figure 4: The energy dispersion in a honeycomb lattice. (a) The valence and conduction bands of graphene derived by the tight binding approximation. (b) The first Brillouin zone of graphene and a contour plot of conduction band. Reprinted from the Ref, [15].

.

As there is no band gap graphene is not suitable for device applications due to the poor on-off ratio. To open a band gap, several methods have been proposed. For instance, quantum confinement in graphene nanoribbons, the generation of strain in graphene, the manipulation of bilayer graphene by electric field and the chemical functionalization of graphene have been suggested to modify the graphene band structure.

2.1.3 Synthesis

Different ways to produce graphene and other 2D materials have been actively researched after the experimental discovery of graphene in 2004 [17]. Mechanical exfoliation from graphite and epitaxial growth on the crystal surfaces are the most common way to produce graphene. Different production methods gives graphene with different qualities, and are thus suited for different types of experiments and applications.

Mechanical exfoliation, first reported by Geim and Novoselov, is probably the simplest method to produce graphene [17]. This method is also known as the 'Scotch-tape' method. In this method, graphite flakes are peeled away from a crystal of graphite by using a scotch tape. This process is repeated until single layer of graphine has been achieved. This method is not selective to the number of layers. Consequently, characterization by optical microscopy and Raman spectroscopy have to be done to distinguish monolayers. Once monolayer graphene sheet has been achieved on the tape, graphene flakes can potentially be deposited on any substrate. SiO_2 coated Si-wafer is one of the most popular choices due to a very particular interface effect which makes it possible to distinguish the number of graphene layers (monolayer, bilayer etc) by optical microscopy. Although the Scotch-tape method gives high-quality graphene, it is laborious and not scalable. Therefore this method is not suitable for industrial applications. However, due to its relative ease, it has been widely used for studies on graphene physics.

Figure 5: The mechanical exfoliation of graphene from graphite via the so called Scotch-tape method. Two transistor made from graphene, a piece of graphite and scotch tape are shown in this image. Photo: Courtesy of the Nobel Museum, Stockholm.

Epitaxial growth of the graphene is the best solution for growing large scale high quality graphene. It has become the most widely used method of graphene production when large-area samples are needed. Epitaxial growth of a material refers to the formation of a crystal on top of a crystalline substrate that exhibits a similar structure. Hydrocarbons such as CH_4, C_2H_4 are mostly used as a source material in a CVD process. At a high temperature, metal substrate acts as catalyst for the decomposition reaction of the precursor gas. The carbon atoms nucleate in multiple position on the surface and form graphene. This process can be done either in ambient pressure or low pressure. The size and shape of the grains and the specific structure of the graphene can be controlled by tuning different growth parameters such as temperature, pressure and exposure times [18]. In addition, the surface morphology also plays an important role on the quality of graphene as the registry of graphene follows the crystallographic orientation of the substrate surface. A lattice mismatch between graphene and the metal substrate can result in the formation of a moire pattern. This stems form the periodically varying registry between the carbon and substrate atoms. If the lattices between grapehne and metal surface are closely matched, there is no moire pattern unless the graphene is rotated. Despite the conceptual simplicity, the details of the growth mechanism of epitaxial graphene depend, among other factors, on the substrate and the temperature. In this work graphene has been synthesized by low pressure CVD process on nickel single crystal. Therefore we discuss in details in the experimental method section.

2.2 Hexagonal Boron Nitride (h-BN)

Hecxagonal boron nitride exhibits the same structure as graphene, and instead of carbon, it is composed of boron and nitrogen. Boron nitride has different forms such as cubic, wurtzite, hexagonal and amorphous. The most stable crystalline form of BN is the hexagonal one [19]. This is also famous for its outstanding properties such as high thermal conductivity,

elasticity, and chemical stability [19]. The A and B lattice sites shown in Figure 2 are occupied by either boron or nitrogen. The lattice constant of h-BN is 2.50 Å which is slightly larger(1.8%) than that of graphene. While graphene is a semi-metal with a zero band gap, h-BN is a wide band gap insulator. The strong difference in electro-negativity between boron and nitrogen atoms leads to opening of a wide band gap of about 5.9 eV.

2.2.1 Synthesis

Similarly to graphene, h-BN has also been mechanically exfoliated as an excellent dielectric material. But this cannot be scaled up similarly graphene. Various h-BN synthesis processes have been demonstrated including precipitation and mechanical exfoliation methods. In addition to these methods, epitaxial growth by CVD process on a transition metal substrate is another route to produce high quality h-BN films. The CVD method has been recently highlighted due to its capability to synthesise large area h-BN with high quality and controllable thickness [20]. h-BN can be synthesised on the metal surfaces using molecular precursors such as borazine ($B_3N_3H_6$) [21], amonia borane(BH_3NH_3) [22] and diborane (B_2H_6) with ammonia [23]. A variety of metal substrates have been tested in the form of foils (Cu [22] [20] [24], Ni [25] and Pt [26]) and metal thin films. Among those, foils are preferred to metal thin films due to their price competitiveness and the advantage of large area synthesis.

The growth of the h-BN on metal surfaces is substantially influenced by the interaction between the metal and precursors. Therefore like epitaxial grapene, the surface adsorption and catalytic activity of metal surface have an important effect on quality of the h-BN. The precursors molecules such as borazine decomposes at high temperature (around 1000°C) in the presence of catalytic metal surfaces, and atomic B and N react to form h-BN. Thus, few layers to single layer of h-BN can be formed on different substrate such as polycrystalline Ni or Cu film [24] [21]. The growth temperature, pressure, deposition time, and precursor dose are important in controlling the quality of the resulting h-BN.

Similar to graphene, the edges of the h-BN island can also be zigzag or armchair terminated. h-BN contains two different elements, which will have an effect on the edge termination. Previous study shows that armchair terminated h-BN edges are typically not be observed [27]. Therefore, the h-BN edges are mostly zigzag terminated and contain either N or B atoms. Recent theoretical studies of growth of h-BN on Cu suggest that triangular h-BN domains with N-terminated zigzag edges are formed as shown in the Figure 6. In the case of a hexagonal domain shape, edges with alternating N and B termination can be observed (Figure 6). B-terminated zigzag edges are not straight while N-terminated edges are always straight and sharp. B-terminated edges are either concave or convex edges depending on the growth parameter such as pressure, temperature etc [27]. The relative stability of the B-terminated edges depends on the substrate. For example, it has been reported that [6] B-terminated edges are more stable than N-terminated edges on Ni(111) substrate.

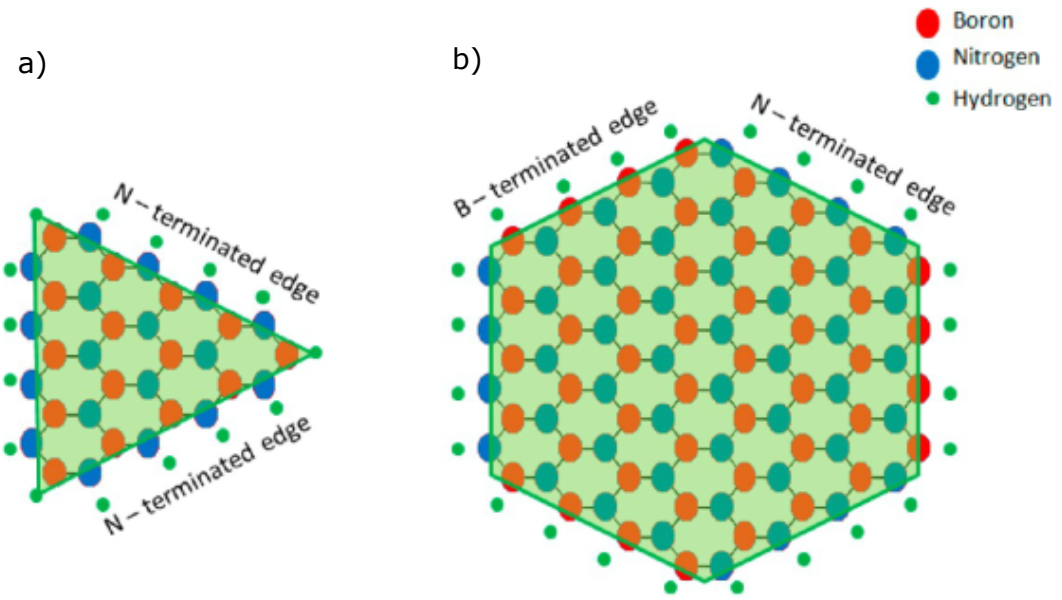

Figure 6: Comparison of atomic arrangement on triangular and hexagonal h-BN domains. (a) Triangular structure with N-terminated edges and (b) hexagonal structure with alternating N and B-terminated edges. Adapted from the Ref [28].

2.3 Moiré Pattern

When two crystalline lattices with slightly different periods superimpose on each other, a periodic superstructure with a repeat distance in the few nanometre range is formed. This periodic superstructure is called moiré pattern. This geometric property arises in almost all graphene systems supported on a crystalline substrate, both in epitaxial and transferred samples. The lattice mismatch between the crystalline over layer and substrate is the main cause of this periodic superstructure [31]. In addition, the rotation between over-layer and substrate can also cause a periodic superstructure. Any physical property on the surface can be expanded in terms of a Fourier-series

$$F^s(r) = \sum_{j,k} c^S_{j,k} e^{i(j\mathbf{G}^S_1 + k\mathbf{G}^S_2)r} \tag{5}$$

where G^S_n are the primitive vectors of the reciprocal lattice of the substrate. Again for the over-layer Fourier-seris is

$$F^o(r) = \sum_{j,k} c^O_{j,k} e^{i(j\mathbf{G}^O_1 + k\mathbf{G}^O_2)r} \tag{6}$$

Now a superposition of the property function $F^s(r)$ of the substrate and $F^o(r)$ of the over-layer can also be represented by an infinite Fourier series with respect to the substrate lattice.

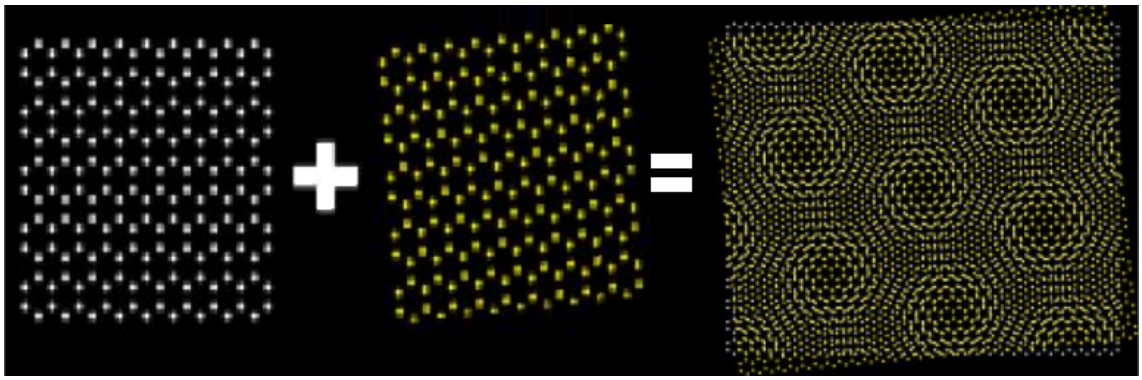

Figure 7: Illustration of the moiré pattern formation: The superposition of a graphene (white) and h-BN (yellow) lattice structure gives rise to a superlattice.

$$\begin{aligned} f_M(r) &= f_S(r) + f_O(r) \\ &= \sum_{j,k} [c^S_{j,k} e^{i(j\mathbf{G}^S_1 + k\mathbf{G}^S_2)r} + c^O_{j,k} e^{i(j\mathbf{G}^O_1 + k\mathbf{G}^O_2)r} \\ &= \sum_{j,k} c^S_{j,k} e^{i(j\mathbf{G}^S_1 + k\mathbf{G}^S_2)r} \left[1 + \frac{c^O_{j,k}}{c^S_{j,k}} e^{i[j(\mathbf{G}^O_1 - \mathbf{G}^S_1) + k(\mathbf{G}^O_2 - \mathbf{G}^S_2)]r} \right] \end{aligned} \tag{7}$$

From the above equation a new periodic structure arises from the superposition and characterized by reciprocal lattice vector G^S_n, G^O_n. The period can be extract by the difference between them:

$$G^M_n = G^S_n - G^O_n \tag{8}$$

Now if we consider the rotation angle between over-layer and substrate lattice is ϕ and the lattice mismatch is δ, the period of the moiré pattern of the graphene on h-BN can be written as [31],

$$d = \frac{(1+\delta)a}{\sqrt{2(1+\delta)(1-\cos(\phi)) + \delta^2}} \tag{9}$$

If $\phi = 0$,

$$d = \frac{(1+\delta)a}{\delta} \tag{10}$$

where a is the lattice constant of over-layer graphene. So, the moiré period depends on lattice mismatch. The angle between moiré pattern and the over-layer depends on the lattice mismatch and the angle ϕ, and this can also be written as [31]

$$\tan\Theta = \frac{\sin\phi}{1+\delta-\cos\phi} \tag{11}$$

For small ϕ,

$$\theta = \frac{\phi}{\delta} \tag{12}$$

This means that the angle of the moiré pattern amplifies the angle between the atomic lattices of the substrate and the overlayer by a factor of $1/\delta$. As the moiré pattern depends on the geometric details of the surface and overlayer structure, detailed information can be extracted from analysis of the superstructure.

2.4 Graphene-hexagonal Boron Nitride hetero-structure

Graphene, with a variety of extraordinary properties including high charge carrier mobility at room temperature, is considered a promising candidate for next generation nano-electronics. However, graphene is a zero bandgap semi-metal. Therefore, bandgap opening for graphene is essential to realize its applications in electronic devices [16]. Recently graphene nano-ribbons and nanomeshes have been suggested as a means to achieve a non-zero bandgap. But the fabrication procedures can introduce defects which cause scattering at the edges, leading to a decrease in the electron mobility. Theoretical calculations have predicted that a bandgap sould open in in-plane Gr/h-BN heterostructures [32] [33].In addition to the the bandgap opening, this heterostructure also has high carrier mobility in the range of $10^3 - 10^5 cm^2 V^{-1} s^{-1}$ [33]. This makes h-BN-G heterostructure a promising 2D material for graphene-based nanoelectronics. Additionally, a lot of fascinating properties have been predicted theoretically for such in-plane heterostructures, such as antiferromagnetism, [34] minimum thermal conductance, [35] and robust half-metallic behaviour. In addition to in-plane heterostructures, graphene and h-BN can also be coupled vertically by interlayer van der Waals interaction to form vertical G/h-BN heterostructures. Some unique physical properties such as Hofstadter butterfly effect has been detected in this heterostructure. Moreover these vertical heterostructures have exhibited higher carrier mobility and better device performance than the traditional graphene based devices [36].

The CVD synthesis of graphitic boron-carbon-nitrogen materials was first reported by Kaner et el. at 1987. After that, one-batch growth of h-BNC hybrid films on Cu foil has been was reported by Ajayan et al [37]. This h-BNC hybrid film contains mixed graphene and h-BN domains having relatively small sizes. This hybrid structure has been characterised by high-resolution transmission electron microscopy (HRTEM) and AFM as shown in Figure 8. These observations indicated that high quality crystalline h-BNC films were synthesized with multiple layers. They also reported that the electrical properties such as electrical conductivity and band-gap of the h-BNC film are strongly influenced by the composition of B, N and C atoms. However, it is difficult to distinguish the graphene and h-BN domains in such highly mixed h-BNC films by TEM. In addition to this method, Park et al. developed a patterned regrowth approach to synthesize monolayer in-plane h-BN-G heterostructures.

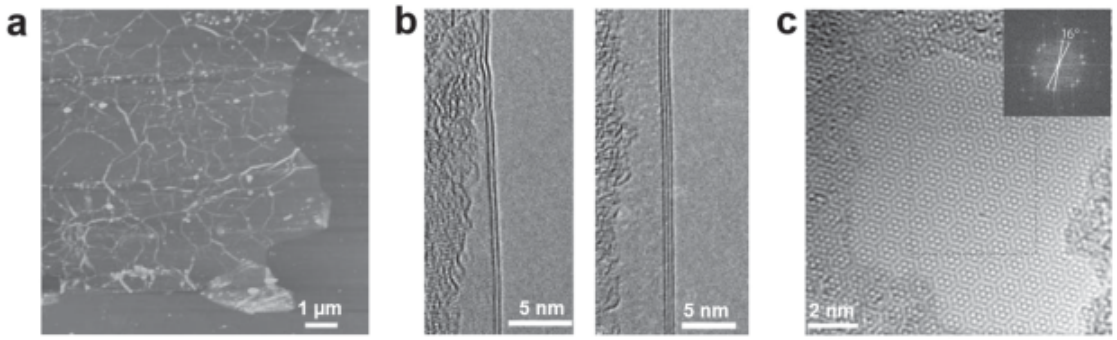

Figure 8: Characterization of the h-BNC film. a) AFM image of the uniform h-BNC hybrids transferred onto a SiO_2/Si substrate. b) HRTEM images showing the cross-sectional view of the h-BNC films. c) Moiré patterns of a two layer packing in the h-BNC films characterized by TEM. Adapted from the Ref [37] .

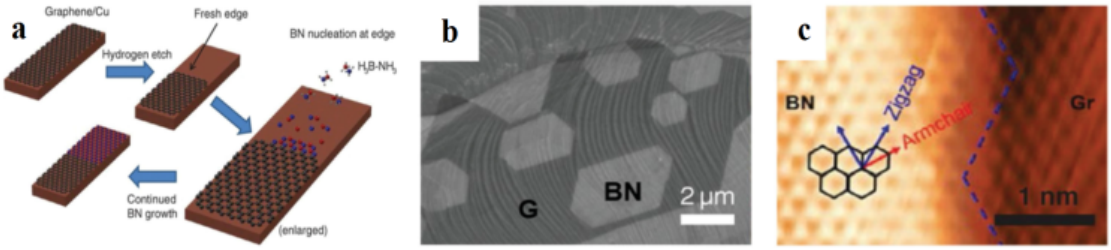

Figure 9: h-BN-G heterostructures growth by pattern regrowth method. a) Schematic diagram of the patterning of the fresh graphene edges by hydrogen etching and subsequent lateral epitaxy of h-BN.b) SEM image of h-BN-G film produced by the growth method shown in (a). c) STM image of an h-BN-G boundary presenting a typical zigzag interface. Adapted from the Ref [11].

In this method, first graphene on Cu is patterned by lithography or reactive ion etcing as shown in Figure 9. After patterning, h-BN is grown on the bare copper substrate regions to achieve a monolayer in-plane h-BN-G heterostructures. This synthetic approach allows to have variable domain shape and sizes in h-BN-G heterostructures. In addition, other lithography techniques such as E-beam lithography, Focused Ion Beam lithography have been used to grow h-BN-G heterostructures [3].

However, the pattern regrowth approach to synthesize heterostructures, cannot be used to achieve precise graphene and h-BN interfaces as lithography induces unwanted structural and chemical disorder on the edges of graphene. Thus the intrinsic properties of the interface would be blurred. In this regard, continuous synthesis of h-BN and graphene, without involving lithography, could generate clean heterostructure interface. A more promising approach to get a controlled interface is the epitaxial, sequential growth of graphene or h-BN on transition metal single crystals. In this case, regular edge structures are obtained, and the edge of the first material will act as a seed for the growth of the second material which leads to a shared lattice orientation. In the in-plane heterostructures, either graphene is embedded in h-BN, or h-BN is embedded in graphene depending on the growth sequence.

Experiments in the past years have focused on well-established transition metal surfaces for graphene growth such as Ir(111) [38], Ru(000) [40], Rh(111) [9] and copper foils. These metal surfaces are also common for synthesising G/h-BN heterostructures. However the moiré pattern on the graphene and h-BN regions on these metal surfaces can be problematic. Even though the lattice constant of graphene and h-BN are very similar, their moiré patterns show larger differences, which leads to strain at the G/h-BN interface. On the other hand, Ni(111) is a suitable metal surface to synthesis such G/h-BN heterostructures as it has closely matched lattice constant with both graphene and h-BN. N(111) is also strongly interacted crystal facet which leads the registry of graphene and h-BN according to 1×1 structure. By subsequent synthesis of graphene and h-BN, atomically sharp interface can be obtained on Ni(111) substrate. The growth temperature of graphene in Ni(111) is lower than h-BN and at high temperature above 600C, graphene growth mode changes from surface-growth to growth by precipitation. For this reason, h-BN is grown before graphene. In this case, the edges of h-BN act as a seed for graphene. Graphene starts nucleating at different spot of the h-BN edges simultaneously. Thus h-BN is embedded in graphene as shown in Figure 10 (a) and (b).

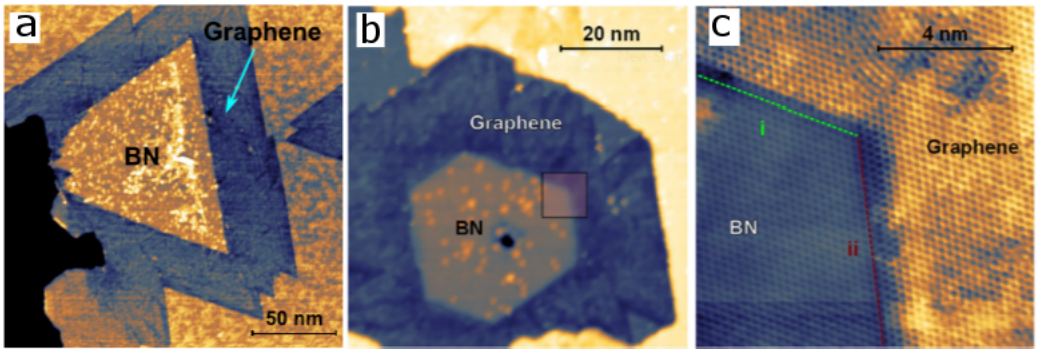

Figure 10: G/h-BN heterostructures on Ni(111). a) BN triangle encapsulated in graphene. b) Truncated BN triangle encapsulated in graphene (1V, 171 pA). c) Atomically resolved STM image of a G-BN structure grown on BN grain with B and N terminated edges. Adapted from the Ref [6].

Previous experiment by Robert et al. [6] shows that the two chemically distinct edges of a hexagonal h-BN island (see Figure 10 (c))are found to be attached with graphene differently. Atomically sharp transition along ZZ direction(interface i shown in the Figure 10) is found while 1 nm wide G/h-BN intermixing transition region is observed in other direction(interface ii shown in the Figure 10). This behaviour depicts that the formation of the either C-B or C-N bonds is preferred on Ni(111) surface. The previous DFT calculation shows that, the C-B and C-N interface energies per bond are estimated about 0.03 eV and 0.09 eV respectively [27]. After graphene growth, C-N interface has also higher energy than C-B interface when the Ni substrate is included. Therefore it is more likely reconstruct to get energetically more stable C-B bonds.

2.5 h-BN-G heterostructures transfer

In order to study electronic properties of a graphene/h-BN heterostructure, it has to be transferred on an insulator from the metal substrate. After synthesis of epitaxial graphene/h-BN heterostructures, transfer of this structure is quite challenging. There are few methods that have already been successfully demonstrated for transferring graphene or h-BN from metal surfaces such as dry transfer methods [41], electrochemical wet etching process [42], electrochemical delamination methods [12] etc. However, transfer techniques for h-BN-G heterostructures are not well-developed, especially in the case of nickel surfaces. The most common way to transfer these kind of 2D materials is the wet etching process. In this method, a polymeric support such as PMMA, PDMS or PC film is used to support 2D materials and the metal film is etched away. The 2D material is supported by the polymer film and floating on the aqueous etchant. This is fished out by tweezers and finally placed on the desired substrate. The last step is the removal of the polymer film.

This transfer method has some disadvantages. Some oxidized metal particles will inevitably be left between graphene and the desired substrate [43]. To avoid this problem, a gentle electrochemical delamination method has been suggested [12]. In this method, the graphene with polymeric support is delaminated from the metal film by the bubbles created by an electrochemical process. The common electrolytic solution that has been used so far is NaOH. A water reduction reaction take place at the negatively charged cathode i.e. the sample. In this reaction, H_2 is produced and creates bubble. The bubbling

starts at the interface of the metal surface and the polymer film and thus, the polymeric support is pushed out mechanically by bubbles resulting in detachment. The polymer film floats on the aqueous solution after the complete detachment. A schematic diagram of the electrochemical cell for bubbling transfer is shown in Figure 11.

In addition to the etching and delamination methods, some research have been done to develop a dry transfer method for graphene [44] [45]. The polymer film used in these methods has to be very thin to make a good attachment with graphene. Then this film has to be supported by an additional stamp or frame. The attachment of graphene to the final substrate may have to be promoted by heating the polymer film.

The complete removal of the polymer film is not an easy task, and several methods for obtaining clean graphene have been demonstrated. Firstly, the polymer film has to be dissolved, and after that thermal annealing is done to remove the water and solvent molecules from the graphene. A number of solvents, such as acetone and chloroform, have been suggested for the first step [46] [47]. In other studies, it has been reported that too quick dissolution of the polymer film may promote cracking of graphene [48]. This can be prevented by changing the solvent gradually to a better solvent for the polymer. Typically, the annealing is done in H_2, Ar, and occasionally O_2 gas mixture. In some studies, elevated temperatures have been shown to lead to decreased charge carrier mobility [47].

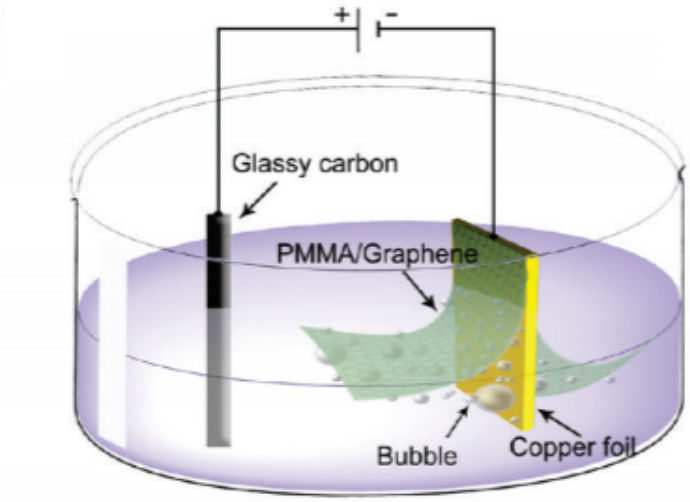

Figure 11: The schematic diagram of electrochemical cell in bubbling transfer of graphene from Cu foil. Adapted From the Ref [12].

3 Experimental Methods

3.1 Growth of Graphene and BN

Efforts to make thin films of graphite by mechanical exfoliation started in 1990, but nothing thinner than 50 to 100 layers was produced before 2004 [49]. Novoselov, Geim and co-workers first demonstrated the electronic properties of graphene obtained by mechanical exfoliation from graphite, in 2004 in their landmark paper. They used normal scotch tape to produce graphene flakes from the graphite bulk by repeated peeling process. By this method they succeeded to produce high quality graphene. This method is favorite for device manufacturing since it is possible to obtain quite large single crystalline graphene flakes with no defects. However this method is not an efficient method to produce graphene as it is time consuming and labor intensive.

While the synthesis of large scale, single crystalline graphene has been challenging, a very straight forward method named chemical vapor deposition (CVD) has been used to make graphene on metal surfaces. The growth mechanism of graphene by CVD method is shown schematically in the Figure: 12. In this method, clean metal surfaces are exposed to hydrocarbons to supply the source carbon atoms for growing graphene. Metal works as a catalyst to break down the hydrocarbon into carbon and hydrogen. Hydrogen atoms leave the surface while the carbon atoms form graphene. We can roughly divide the graphene growth mechanism into two different paths depending on the solubility of carbon atoms into the bulk metal as shown in the Figure: 12. Solubility of carbon atoms in the substrate is typically a function of temperature, with increasing temperature resulting in increased solubility. If the carbon atoms are not soluble in bulk metal at the graphene growth temperature, they remain on the surface and therefore aggregate to form graphene. On the other hand if carbon atoms are soluble into bulk metal at growth temperature, then they segregate to the surface while sample is cooled down. Graphene is formed upon segregation to the surface. The carbon solubility of Ir, Pt, Pd, Cu Ru and Rh [50] at the growth temperature is low. Therefore, on these surfaces, graphene forms through the on-surface growth path. As previously mentioned, metal surfaces act as a catalyst for decomposition of hydrocarbon. Therefore once graphene covers the metal surface ,no more active sites are available for the decomposition reaction, and the graphene growth self-terminates once a full monolayer has been reached. There are some other transition metals such as Ni [51] [52] , where the solubility of the carbon is high at the graphene growth temperature. After decomposition of hydrocarbon, the carbon atoms go into the bulk nickel at high temperature, and when sample is cooled down they come out on the surface to form graphene. In this case, the growth is not self limiting as the surface remain active at high temperature. Therefore the thickness of the graphene layer would not be limited to a monolayer.

However in this experiment we used Ni single crystal as substrate to make graphene and h-BN heterostructures. The synthesis of graphene and h-BN on Ni(111) has been done by using CVD method in UHV. In this method, nickel substrate has been exposed into hydrocarbon i.e ethylene at high temperature in UHV. The growth of epitaxial graphene on Ni(111) depends on multiple factors including temperature and presence impurities in the near surface of the Ni(111).

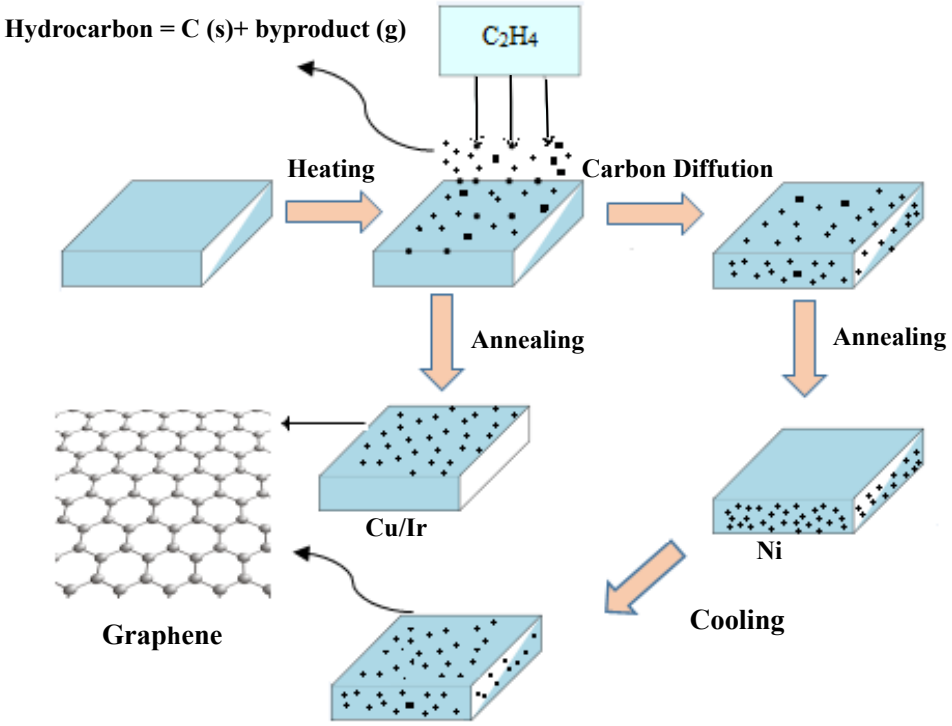

Figure 12: Schematic diagram of epitaxial graphene growth mechanism on transition metals by CVD method.

As mentioned earlier, the solubility of the carbon increases with the annealing temperature. On the Ni(111) surface, graphene is thus not stable at temperatures exceeding 600° C [53]. On the other hand, exposure of the surface to a hydrocarbon below 500°C results the formation of nickel carbide [54]. There is a temperature window between these values, where the epitaxial and self-terminating growth of graphene on Ni(111) is possible [53].

The experimental procedure for graphene synthesis can also be applied for BN. In the case of BN synthesis by low pressure CVD process, the source materials such as ammonia borane (BNH_6) or borazine ($B_3N_3H_3$) are preferred as precursor molecule. In this experiment we used borazine as a source material of B and N atoms. The growth temperature of BN on Ni(111) starts from 800°C. The borazine gas was leaked into the UHV chamber at 10^{-8} mbar. The hot Ni (111) sample was exposed to the precursor gas for 5 to 10 minutes. The borazine breaks down into B and N by decomposition reaction while the metal surface acts as catalyst. The B and N remain on the metal surface and forms h-BN by attaching each other. Contrary to the graphene, BN form characteristics triangular domain on the substrate. The edges of the BN island can act as seed for growing graphene afterwards [6].

3.2 Auger Electron Microscopy

Auger electron spectroscopy (AES) is one of the most commonly used techniques for elemental analysis in surface physics. It was developed in the late 1960s. In the Auger

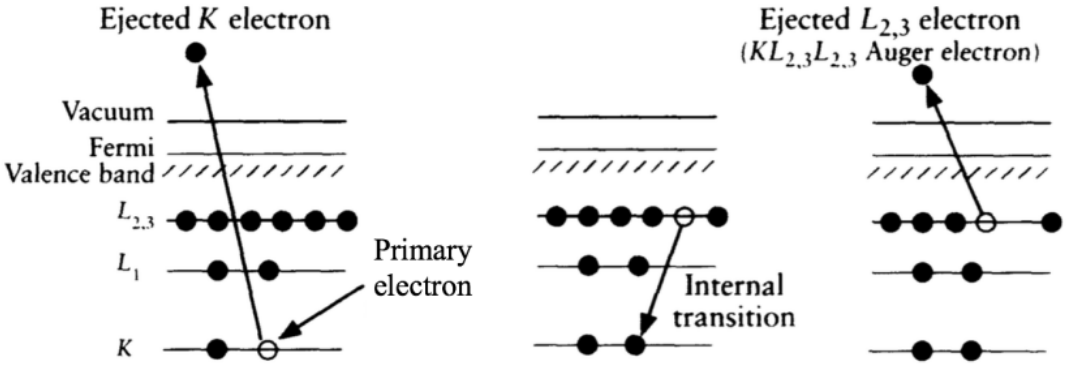

Figure 13: Relaxation of the ionized atom by Auger process, adapted from Ref [55].

process a beam of electrons is focused on the target surface. The energy of the emitted electron beam varies from 2-10 keV. When the primary electron hits the surface, a core hole is created on a lower energy level of a surface atom. The ionized atom is now in an excited state and will rapidly relax back to a lower energy state by two mechanisms. One way is the emission of the characteristic X-ray photon (fluorescence), and the other way is the emission of an Auger emission. The hole created by emission of primary electron is filled by an electron from a higher energy level and thus, an x-ray is emitted. Alternatively, the energy can be transferred to an electron on one of the outer energy shells leading to the emission of a characteristic higher energy electron. The electron emitted in the latter case is called an Auger electron (AE). The basic principle of Auger process is shown in the Figure 13.

The kinetic energy of an Auger electron can be approximated by a difference of the energy levels involved in the process. For example, for the process depicted in Figure 13, the energy of the Auger electron is approximately given by

$$E_K = E_K - E_L - E_L - \phi \tag{13}$$

Where $\phi = E_{vacuum} - E_{fermi}$ is the work function of the material. Equation 13 shows that the Auger electron energy is a function of the atomic energy levels. The atomic energy levels are specific for each element therefore the kinetic energy of the Auger electrons can also be specific which allows AES to be used for elemental identification. In this work AES was an effective tool by which we can easily analyse the chemical elemental information on the metal surface and also can estimate the surface coverages by comparing the AES differential peaks height. The AE intensity is plotted against kinetic energy of incident electron as shown in the Figure 14.

The basis for the Auger electron peak height analysis is that the AE signal from a substrate material decays exponentially as the thickness of a uniform overlayer increases [56]. The AE signal of a substrate through an uniform overlayer can be written as

$$I_s = I_s^{\alpha} exp(-d/\lambda_s Cos\theta) \tag{14}$$

Where I_s is the substrate AE signal intensity, I_{α}^{s} is the AE signal intensity from a clean, infinitely thick substrate, d is the thickness of the overlayer, λ_s is the electron attenuation

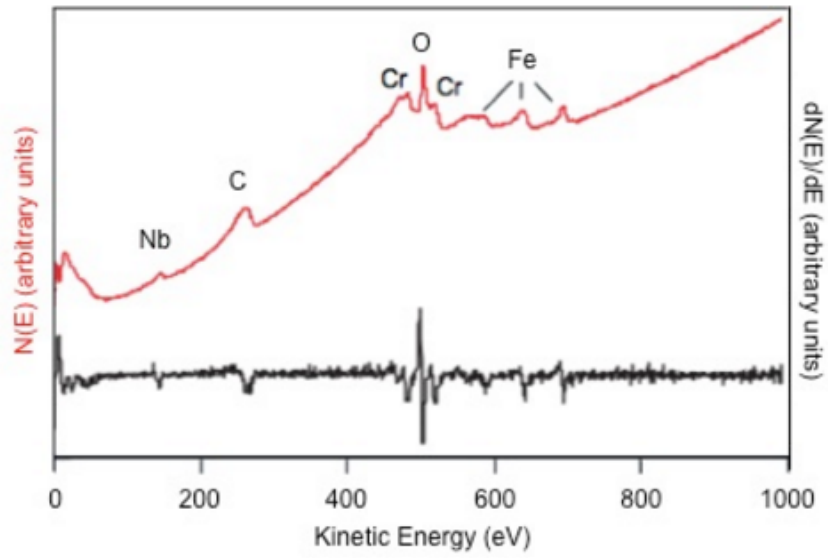

Figure 14: AES direct spectrum (red) and differentiated spectrum (black) of an oxidized Fe-Cr-Nb alloy, adapted from Ref [57].

length of the substrate AE and θ is the escape angle of the AE with respect to the surface normal resulting from the analyser geometry. For the overlayer intensity

$$I_j = I_j^{\alpha} exp(-d/\lambda_j cos\theta) \tag{15}$$

The AE signal from the infinitely thick samples can be written as follows

$$\frac{I_1^{\alpha}}{\rho_1 S_1} = \frac{I_2^{\alpha}}{\rho_2 S_2} \tag{16}$$

where ρ_i and S_i are the density and sensitivity factor of the element, respectively. Using this relation we can write the intensity ratio as,

$$\frac{I_s}{I_j} = \frac{\rho_s S_s}{\rho_J S_j} \left[exp(\frac{d}{\lambda_s cos\theta}) - exp(\frac{d}{cos\theta}(\frac{1}{\lambda_s} - \frac{1}{\lambda_j}) \right] \tag{17}$$

From the above Equation 17 we can see that AE peak height ratio correspons to AE signal intensity ratio, and hence the overlayer thickness d can be solved numerically. The escape angle of the AE for cylindrical mirror analyser used in the experiment was $\theta = 42.3°$.

3.3 LEED

The discovery of the electron's wave nature was a milestone in the development of the modern physics and eventually it was achieved by the LEED (Low Energy Electron Diffraction) like experiment. Low energy electrons are much more sensitive to the surface than bulk as the mean free path is extremely short and low-energy electrons cannot penetrate deep into the bulk without undergoing inelastic scattering. In contrast for higher energy electron can get refracted through the surface into bulk easily as it has higher energy. In

other way, the inelastic mean free path for low energy electrons in solid is short. Therefore, low energy electron based experimental techniques are surface sensitive. There are two main applications of the LEED . The first one is to analyze the diffraction pattern obtained from the surface inspection. This gives immediate and direct information about the surface order and quality. It also gives immediate information about the surface symmetry and periodicity when surface is reconstructed or covered with an ordered adsorbed layer. The second application is quantitative structure determination which is more difficult to interpret. One has to measure the diffraction intensities as a function of the electron kinetic energy. The results are then compared with the sophisticated multiple-scattering calculation for a model system. Despite of this complexity LEED is the most important experimental tool for quantitative surface structure determination.

3.3.1 Instrumental Setup

The following Figure: 15 shows a typical instrumental set up of the LEED system. The LEED system has two major components a) an electron gun which produces a beam of monochromatic electrons and b) a detector which detects elastically scattered electrons. An electron gun creates a collimated electron beam that has a precise kinetic energy. A sufficient voltage is applied between two electrodes in vacuum and therefore electrons are emitted from the filament. The detector system of the LEED is much more complicated. The detector consists of four metal grids at different voltages and a fluorescent screen. The first two grids are connected with the ground potential and the next two grids are set with a voltage called retarding potential. This voltage is slightly lower than the kinetic energy of the electrons produced by the gun. It repels almost all the inelastically scattered electrons. Therefore elastically scattered electrons can pass through the next grid which is grounded again. As the fluorescent screen is set to a high voltage, the elastically scattered electrons are accelerated towards it. These elastically scattered electrons hitting the screen give rise to light emission that is intense enough to be observed by the naked eye. Behind the screen there is a view port in the vacuum system so that the LEED pattern can be observed directly or recorded with a camera.

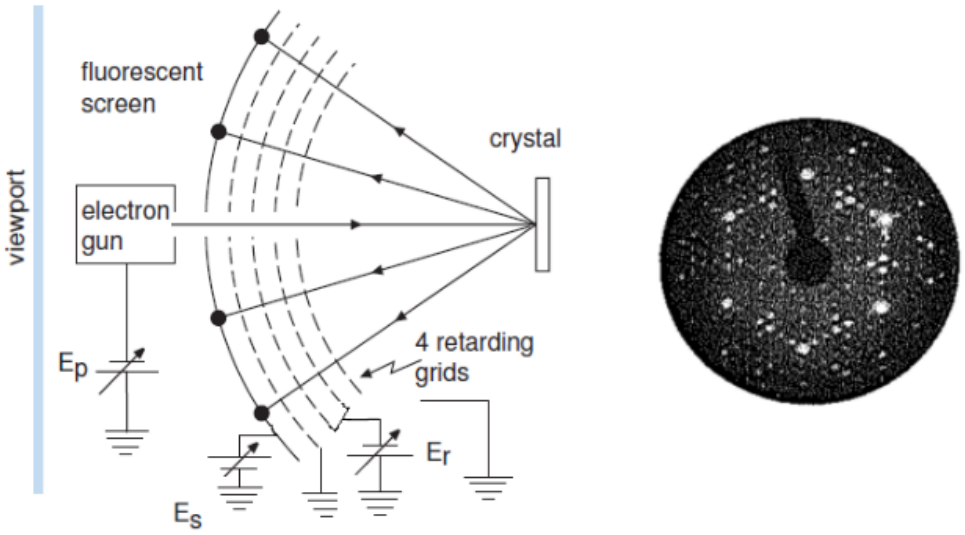

Figure 15: Schematic diagram of a standard four grid LEED set up and a LEED pattern of a Si(111)(7×7) as seen on the fluorescent screen, adapted from Ref [58].

3.3.2 LEED Diffraction Pattern

We already discussed the importance of using low-energy electrons to get the diffraction pattern of 2D surface. The atomic diffraction can only occur when electron wavelength is on the order of or less than the inter-atomic distances. The de Broglie wavelength of an electron is given by

$$\lambda = \frac{h}{\sqrt{2mE}}, \lambda\,[] = \sqrt{\frac{150}{E(eV)}} \tag{18}$$

For a typical range of energies used in LEED (30-200eV) the wavelength of the electron is 1 -2Å which satisfies the atomic diffraction condition. The diffraction conditions for a two-dimensional lattice are given by the Laue condition

$$\vec{K}_s^{\parallel} - \vec{K}_i^{\parallel} = \Delta\vec{K}^{\parallel} = g \tag{19}$$

where $\vec{K}_i^{\parallel}$ and $\vec{K}_s^{\parallel}$ are the components of the incident (k_i) and scattered (k_s) electron wave vectors parallel to the surface and g is a surface reciprocal lattice vector. The momentum of normal to the surface is not conserved in this process. The law of conservation of momentum concerns only the wave vector components which are parallel to the surface. In other word, the scattering components parallel to the surface, ($\vec{K}_s^{\parallel}$ - $\vec{K}_i^{\parallel}$) must be equal to the surface reciprocal lattice. This can be visualized by Ewald construction which is illustrated in the Figure 16. It starts by drawing a circle with a radius of $\left|\vec{K}_i\right|$. Then, a vector $\vec{K}_i$ is drawn that terminates at a reciprocal lattice point. The intersection of this circle and the reciprocal lattice points gives the possible final K_s vector, for which the constructive interference is observed. The Edwald construction for bulk and surface are shown in the Figure 16 (a) and 16 (b) respectively. The discrete points in the Ewald construction for bulk are replaced by rods for the surface case as there is no Laue condition perpendicular to the surface. This can be also justified by saying that the real-space periodicity in the

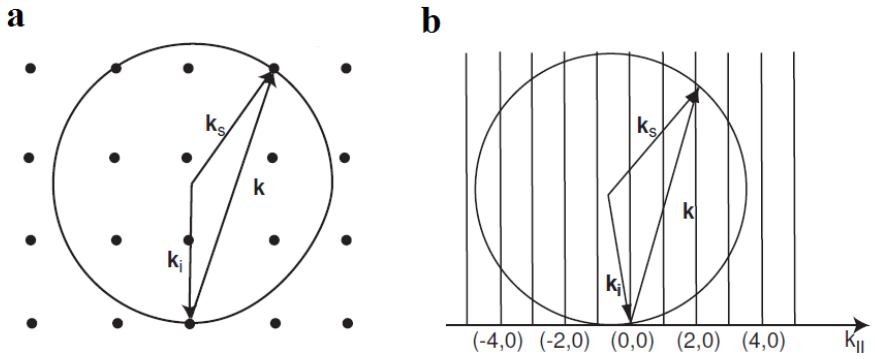

Figure 16: The Ewald construction for (a) the bulk case (b) 2D surface lattice [58].

thirddimension is infinite, which means the reciprocal lattice points have to be infinitely close to each other, forming the rods.

3.4 Scanning Tunnelling microscopy

3.4.1 Basic Principle and Imaging

Scanning Tunnelling Microscopy (STM) is an important experimental method in physics by which individual atoms can be imaged and manipulated. During early 80s, STM was invented at IBM Zurich Laboratory by Gerd Binnig and Heinrich Rohrer [59], who were awarded the Nobel Prize in Physics in 1986 for their spectacular invention. Now STM is a well established method in surface physics. The standard resolution of the STM images is considered to be 0.1 nm lateral resolution and 0.01 nm depth resolution [60]. STM can not only be used in Ultra-high-vacuum but also in ambient air, water, and various other liquid or gas environments and at temperatures ranging from near zero kelvin to a few hundred kelvin [60]. The basic working principle (see Figure 18) of STM is based on the quantum mechanical phenomenon of tunnelling. When a metal tip is brought close to the surface and a bias voltage is applied between them, electrons can pass from the tip to the sample or vice versa through the vacuum by so called quantum tunnelling. The air gap or vacuum behaves as the barrier for the electrons . when this vacuum or air gap is thin enough, electrons can pass through this barrier. This would not occur according to classical mechanics, but can take place with a certain probability in quantum mechanics. In quantum mechanics electron can be described by the wave function $\psi(x)$ which satisfies the Schrödinger equation. The probability of finding the electron at point x can be evaluated by calculating the square of the wave function. Now if we consider a potential barrier shown in Figure 17 which is time-independent and one-dimensional, then the Schrödinger equation can be written as

$$-\frac{\hbar^2}{2m}\frac{\mathrm{d}^2}{\mathrm{d}x^2}\psi\,(x)) + U(x)\psi(x) = E\psi(x) \tag{20}$$

where $\hbar$ is the reduced Planck constant, x the position, $U(x)$ the potential along x direction, m is the mass of the electron and E the energy of the electron. In this approximation, there are two possible regions with $E > U$ which refers outside of the potential barrier and

$E < U$ that is inside the potential barrier. In classical physics the electron with $E > U$ can propagate. The solution of the classically allowed region are plane waves of the form

$$\psi(x) = \psi(0)e^{\pm ikx} \tag{21}$$

where k is the wave vector, given by

$$k = \frac{\sqrt{2m(E-U)}}{\hbar} \tag{22}$$

In equation 21, ± represent that the direction of the plane wave. Equation 20 can also be solved inside the potential barrier which is classically forbidden region for the electron. The solution in the barrier can be written as

$$\psi(x) = \psi(0)e^{-\alpha x} \tag{23}$$

where decay constant is given by

$$\alpha = \frac{\sqrt{2m(U-E)}}{\hbar} \tag{24}$$

Now taking the square of the equation 21 we can find the probability of the electron behind a barrier of width x

$$\frac{|\psi(x)|^2}{|\psi(0)|^2} = e^{-2\alpha x} \tag{25}$$

and the tunneling current I can be written as

$$I = I_0 e^{-i2\alpha x} \tag{26}$$

where I_0 is current inside of the barrier. To make a simple approximation , the Fermi levels on either side of the barrier are considered to be aligned(figure 17) so that no net current will flow through barrier as it is equally likely for the electron to tunnel left to right or right to left. Now if voltage difference is applied across the barrier, a net tunneling current flows through the barrier. The current flowing between metal tip and sample depends on the decay constant α exponentially . The value of α is order of $Å^{-1}$, that is, the tunneling current changes by an order of magnitude per Ångström. This means that tunneling current is very sensitive to the barrier width i.e. tip-sample distance.

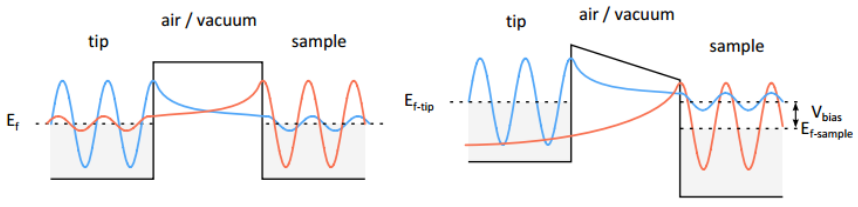

Figure 17: A simple model for the tunneling junction between the STM tip and the sample. a) No bias voltage is applied between STM tip and sample. b) A small bias voltage is applied. Blue line represents a plane electron wave tunneling from the tip to the sample and the red curve from the sample to tip. Adapted from the Ref [61].

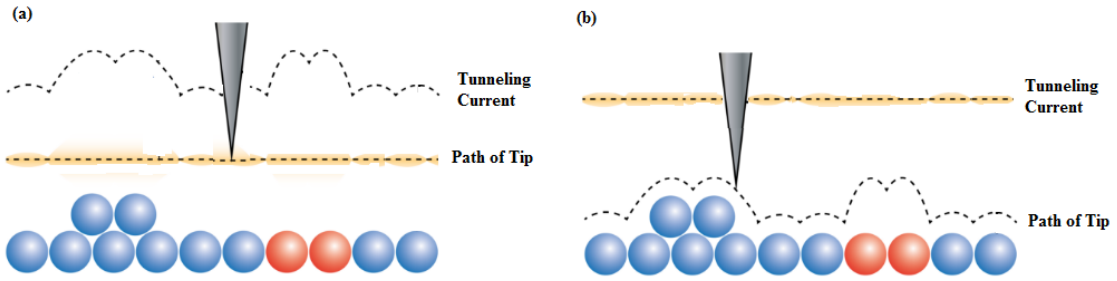

Figure 18: Basic working principle of STM imaging. (a) Constant height mood. (b)Constant current mode. Adapted from the Ref [61].

The condition of the surface of the sample during scan is important as tunnelling is achieved at very small distances. To avoid accidental contact between sample and tip, the sample surface should be as clean as possible. For this reason STM is most often performed on single crystalline samples that have been cleaned in UHV before imaging. The most commonly used imaging method is the constant current mode on which the tip is raster scanned over the surface in xy direction. Meanwhile a feedback loop keeps the tunnelling current constant by adjusting the the tip-sample distance in z-direction. The feedback output, i.e. the movement of the tip in z-direction, is recorded and gives the real space topography over the raster scanned area. Besides this there is another mode of imaging named constant height mode. In this mode, the tip height is kept constant during scanning. The changes of the tunnelling current gives the topography of the surface. Electronic properties of the sample surface also have an effect on the measured current. In Figure 18, the two red color atoms represent substituent atoms with different electronic properties compared to the neighbouring atoms. Therefore for these two atoms, the feedback loop i.e the tunnelling current (Figure 18.a) and the tip distance (Figure 18.b) shows corresponding response due to the changes in the local density of states.

Experimentally, the tip needs to be moved very accurately both vertically and laterally. This is achieved by moving the tip or sample with piezoelectric crystals. The lattice strain in a piezo crystal can be controlled by an external electric field. The piezoelectric controller transforms a voltage into contraction or expansion of a piezo crystal, enabling very precise movement. Several mechanical designs for a scanner have been proposed. The most common one is the tube scanner. Due to the extreme sensitivity of the tunnelling current to the tip-sample distance, vibration isolation and a rigid STM design have to be applied. Typical methods for vibration isolation are suspension-spring systems and eddy-current damping. The schematic diagram of the working principle is illustrated in the Figure 19.

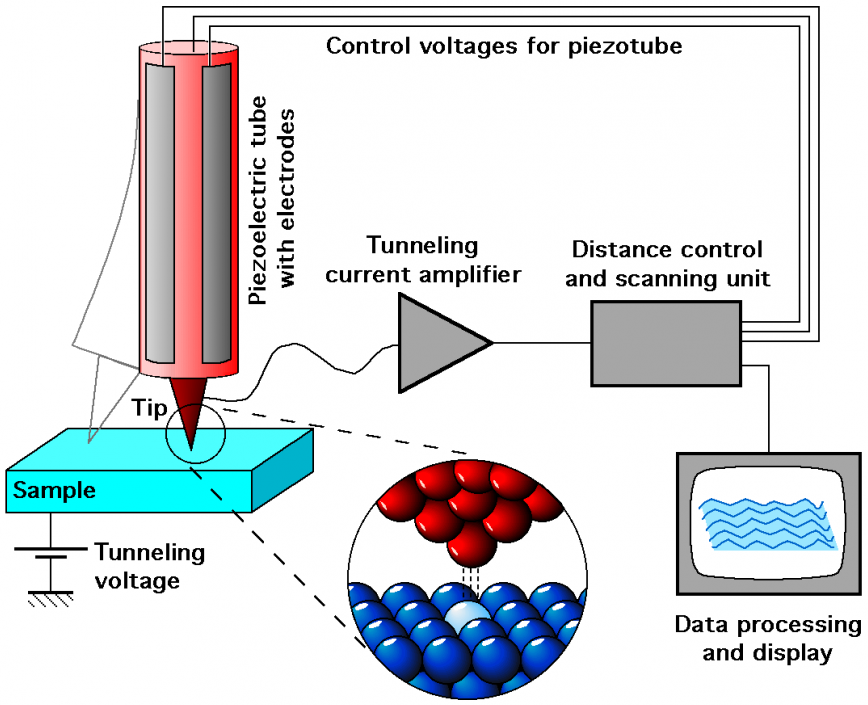

Figure 19: A schematic representation of an STM. An STM setup includes a scanning tip, a piezoelectric controlled scanner, tunneling current amplifier and a computer. Adapted from Ref [60].

3.5 Raman Spectroscopy

Raman spectroscopy is a vastly used method to identify different nanomaterials including graphene and h-BN. Raman spectroscopy provides information on defects and thickness of the material. In our experiment Raman method was used to identify graphene and h-BN after transfer onto silicon (SiO_2) wafer. In Raman spectroscopy, the inelastically scattered light comes from the sample is used. To understand Raman spectroscopy of graphene (and other 2D materials), we have to consider the phonon dispersion of these materials. In graphene with the two-atom unit cell, there are six different phonon dispersion branches. Three of them result from acoustic (A) and other three are generated from optical phonons (O). For one A and one O phonon branch, the vibrations are perpendicular to the lattice plane, and for two A and two O branches, the vibrations are in plane. Additionally, the branches can be classified as either longitudinal or transverse with respect to the carbon-carbon bond direction. Thus, the six phonon bands can be labelled as shown in the Figure 20(a) [62] [63].

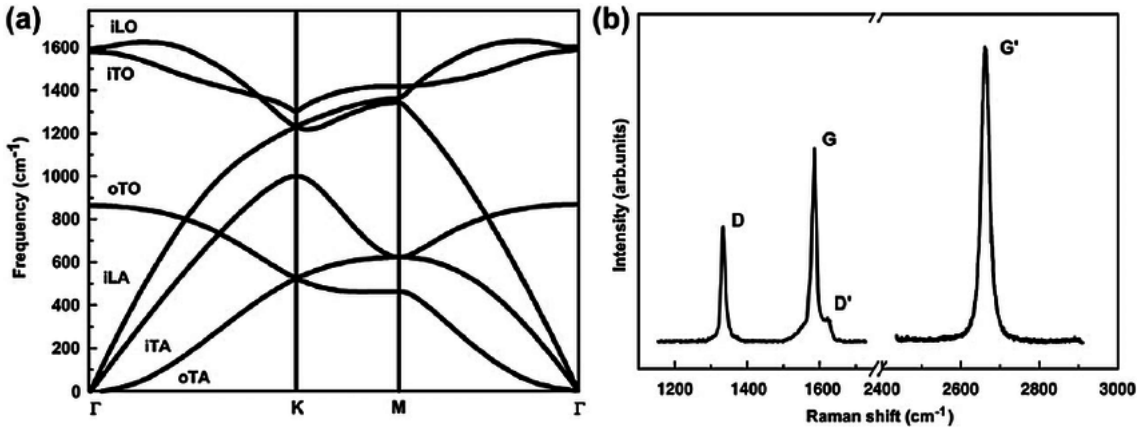

Figure 20: (a) Calculated phonon dispersion relation of graphene showing the LO, iTO, oTO, LA, iTA, and oTA phonon branches. (b) Raman spectrum of a graphene edge, showing the main Raman features, the D, G and G' bands taken with a laser excitation energy of 2.41 eV [63].

The most prominent features of graphene Raman spectrum are the so called G peak at 1580 cm^{-1}, a G' (also denoted as 2D) peak at 2700 cm^{-1} and in the presence of defects, a D peak at 1350 cm^{-1}. The G peak is associated with doubly degenerate phonon mode and it comes from the normal first order Raman scattering. The G' and D bands originate from a second-order scattering process. In the case of G', two iTO phonons near the K point are involved, and in the case of the D band, one iTO phonon and a defect are involved [63]. Monolayer and bilayer graphene are difficult to distinguish by optical microscopy, but in Raman spectroscopy they have different signatures. In the spectrum of bilayer graphene, the G' (shown in the Figure 20(b))peak is clearly broader than in monolayer graphene. In the case of bilayer graphene, both the electronic and the phonon bands are split into two components with special symmetries. A typical Raman spectrum of CVD grown monolayer graphene is shown in Figure 20(b).

h-BN can also be detected by Raman spectroscopy. In Raman spectrum of h-BN, the characteristic peak is seen at 1369 cm^{-1} wave number. Figure 21 shows the Raman spectra for graphene (black), h-BN (blue) and G/h-BN interface (red).

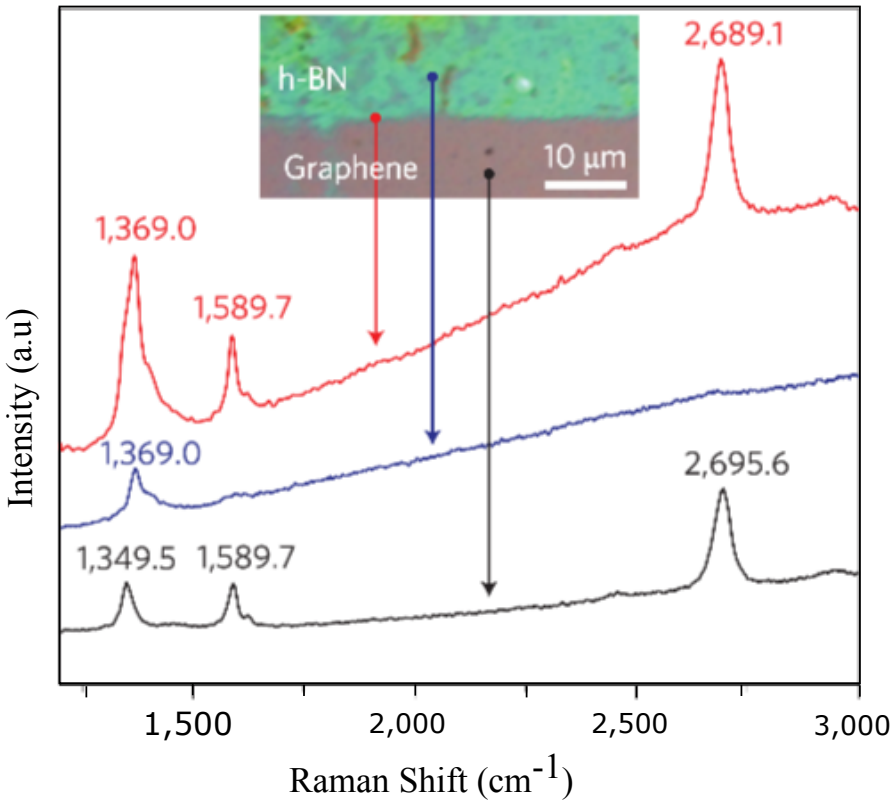

Figure 21: Raman spectra of graphene , h-BN and G/h-BN interface. Adapted from the Ref [3].

3.6 Electrochemical Bubbling transfer

After the synthesis of graphene, h-Bn or G/h-BN heterostructures, it is necessary to transfer them onto another substrate like insulator for further study of their electrical properties. As discussed earlier, among all the transfer mehods, electrical delamination is a promising approach as it is comparatively easier, non-destructive and cost-effective. The whole process of electrochemical bubbling transfer method is shown schematically in Figure 22

The sample has to be part of an electrochemical cell for the bubbling transfer. Typically aqueous NaOH solution is the most commonly used electrolyte in bubbling transfer method. The heterostructure / Ni(111) is used as cathode, and Pt coated silicon is used as anode to avoid unwanted side reaction in this process. Anode is dissolved in this electrochemical process and hence the cathode can be contaminated by adsorption of unwanted materials. For this reason a less reactive material such as Pt is used as anode to avoid unwanted contamination of Ni(111). The half equations are written as

$$4H_2O + 4e^- = 2H_2 + 4OH^-(cathode) \tag{27}$$

$$2H_2O - 4e^- = O_2 + 4H^+(anode) \tag{28}$$

The rate of the reaction at both the anode and the cathode depends on the concentration of the solution and applied voltage. We optimized the rate of bubbling by using 0.25 mol/L concentration and a suitable applied voltage on the cell. For this arrangement the bubbling at cathode starts above 1.2V. We kept the applied voltage at around 2.7V to get a decent

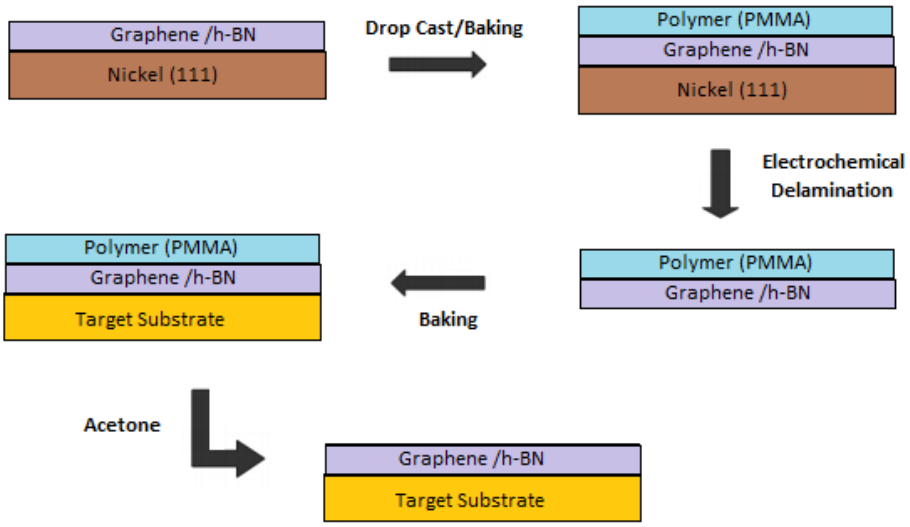

Figure 22: Graphene transfer process by Electrochemical delamination process.

bubbling rate for our heterostructure. Prior to the bubbling transfer, G-hBN/Ni(111) is coated with a polymer support. PMMA (polymethyl methacrylate) is used for coating the heterostructure. For bubbling transfer methods, the thickness of the polymer support might play an important role. With a very thin polymer support, the heterostructure might be strained easily and would be difficult to fish out after detachment. For a very thick polymer support , the polymer stamp does not adhere to G-hBN properly, and hence it comes out leaving the heterostructure in the Ni(111) surface during bubbling. To get an optimum thickness, polymer film was made by drop-casting method. A drop of PMMA (950 A3) is deposited on the sample and baked on a hotplate at 120 ° for 1 minute. After finishing baking, the polymer/ G-hBN / Ni(111) sample is immersed in aqueous NaOH solution as cathode. The bubbling starts when the applied voltage between anode and cathode increases above 1.2V. Voltage between 2.5V to 2.8V gives a gentle bubbling rate. The bubbles are created on the G-hBN and Ni(111) interface, and these bubbles apply a mechanical force on the polymer film to detach from the crystal surface. The bubbling starts from the edge of the polymer film and it continues spreading across the whole area. After 5-15 minutes, the whole polymer film comes totally off the Ni(111) surface.

When the heterostructure and polymer support are completely separated from the Ni(111) surface, the sample is picked up and rinsed carefully in deionized water. The sample is floating on the solution after detachment, and it is difficult to handle by tweezers due to the thinness of the film. To make this task easier, we put a polymer scotch tape on top of polymer film so that sample can be handle easily by tweezers. However after rinsing the sample with deionized water, we transferred it onto the targeted substrate (Si with about 300 nm SiO_2). This silicon substrate with the sample was baked at 120°C for two minutes so that the polymer film attaches better with the substrate. The sample was kept in acetone solution for 24 hours to remove PMMA from the heterostructure. Alternatively, to increase

the dissolution rate, PMMA is removed by acetone at 5O°C. Once PMMA completely dissolved in acetone, sample was rinsed with isopropanol to remove the remaining acetone from the sample.

4 Result and discussion

4.1 Graphene and h-BN growth on nickel thin film

The goal of this experiment was to make atomically well-defined and extended graphene/h-BN interfaces, and transfer the samples onto other substrates after growth. Ni thin film is suitable substrate especially for transferring heterostructure synthesized on it. Ni thin film was made on top of Ir single crystal. By definition, thin film is a layer of material with thickness from a fraction of nanometers to several micrometers. There are a couple of typical techniques which can be used to make thin films such as chemical deposition and physical deposition. An active chemical reaction take place on the target surface in Chemical Deposition method, while in Physical Deposition method the atoms of the film material are deposited directly on the target surface. In this thesis work we used physical deposition method for making nickel thin film. The Omicron EFM3 e-beam evaporator was used to deposit Ni onto clean Ir single crystal. The Ir single crystal was first cleaned by sputtering with Argon gas ions for 10 minutes and annealed it at around 1200C temperature for 5 minutes. The flux of evaporated Ni was set to a constant value of 100 nA, and the cleaned Ir(111) sample was exposed for 20 minutes. According to the previous experiments, about 3.5 nm thick Ni film can be obtained with this set of parameters. The terraces of nickel thin film cannot be seen clearly (see Figure 23(a)) in STM images which were taken right after nickel deposition. But the size of terraces increases, once sample is annealed at high temperature (see Figure 23(b)). To check the crystal orientation of the thin film surface, we took LEED images. The LEED image shown in the Figure 23(d) (inset) indicates that, the nickel thin film surface is terminated by Ni(111) single crystal orientation. AES measurement has also be done to check the surface coverage of the Ni film on the Ir(111) surface. The ratio of the differential peak height between Ni and Ir was 3.6. Using this value into equation 17, the thickness of the nickel thin film can be measured. The average thickness was measured about 35 nm to 50 nm. A large scale STM image (10×10 μm^2) shown in the Figure 23(d) depicts that, thickness of the nickel film was not uniform. There were some nano pillar of nickel that have a height of 50 nm to 80 nm height.

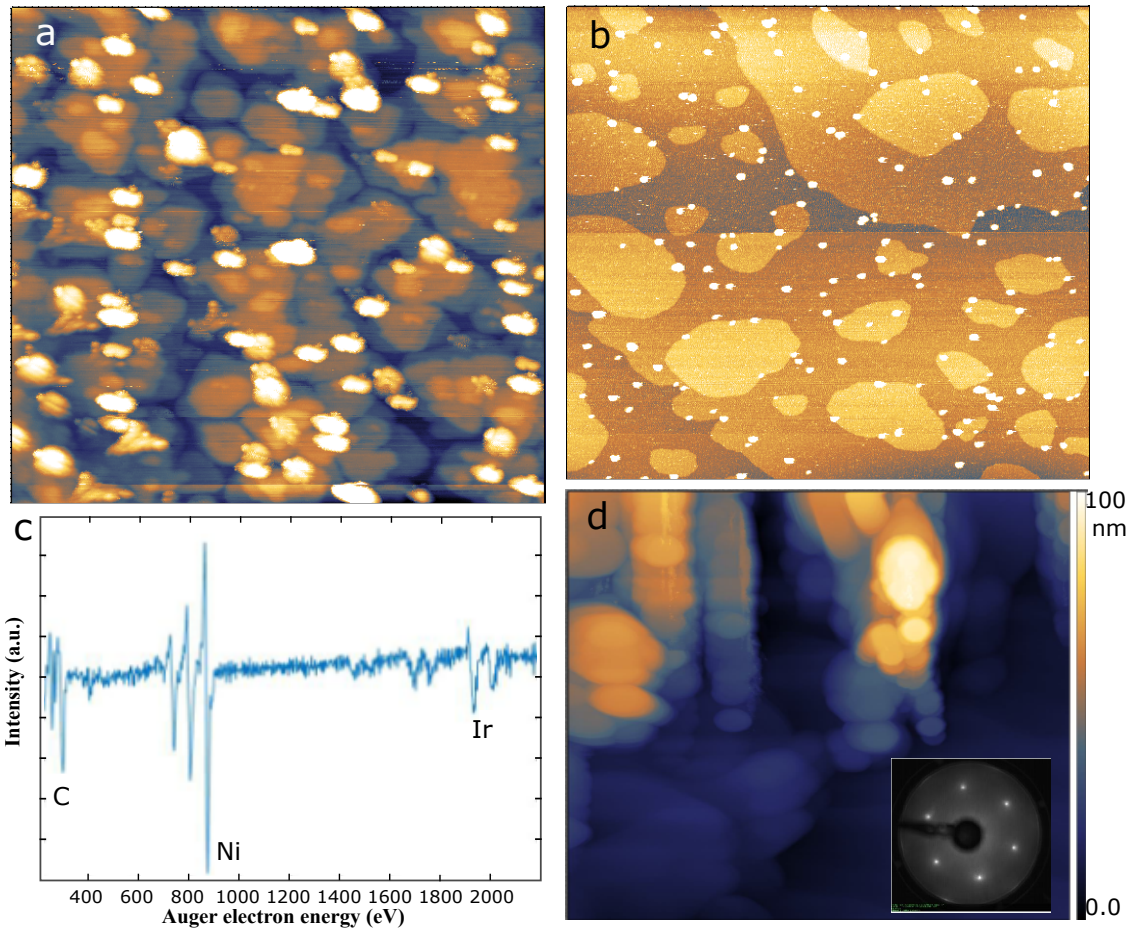

Figure 23: a) STM image (200×200 nm^2) of Ni thin film surface before annealing. b) STM image (200×200 nm) of Ni thin film surface after annealing. c) AES graph after nickel thin film deposition. d) STM image (10×10 µm) of Ni thin film surface and the leed pattern of Ni thin film after annealing.

The solubility of carbon in nickel is very high. Therefore, nickel film can be contaminated easily by carbon atoms from impurities and this contamination might have an effect on the growth of graphene. The white spots on the Figure 23(a,b) might be caused by carbon contamination. There is an AE differential peak at 275 eV electron kinetic energy (23(c)), demonstrating the presence of the carbon contamination. Density of carbon contamination on the nickel surface can also be estimated by comparative AE differential peak height analysis. Carbon contamination can be removed by oxygen treatment. The nickel surface is exposed to oxygen gas at high temperature and the carbon species on the nickel surface is burnt away. In this experiment, oxygen gas is leaked into UHV chamber through leak bulb at low 10^{-6} mbar pressure for 30s. If this unwanted carbon contamination is not removed, it can form graphene on the nickel surface after annealing (through the precipitation upon cooling mechanism). We have noticed moiré pattern of graphene (see Figure 24(a)) on nickel thin film before oxygen treatment. As the lattice constant of graphene and nickel are almost same, the moiré pattern between them should not be seen unless the nickel surface is strained and distorted. From this moiré pattern we can estimate the rotation angle between graphene and nickel surface. The periodicity of the moiré pattern is about 5 nm and the calculated angle of rotation is about 3 degree. However, as indicated above, we can

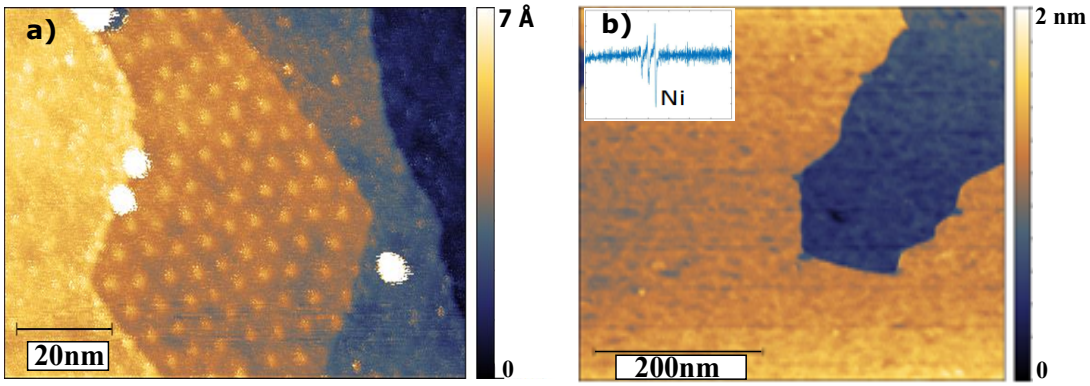

Figure 24: Nickel thin film surface. a) Before oxygen treatment. b)After oxygen treatment.

remove this additional carbon arising from contamination by the oxygen annealing method. The AES graph (see Figure 24.b (inset))shows there is no AE peak for carbon, and STM image (see Figure 24(b)) also indicates that the oxygen treatment has removed the carbon contamination from the nickel surface.

Once we get a clean nickel surface, graphene is grown on this. To synthesize graphene, clean nickel surface was exposed to ethylene in low 10^{-7} mbar pressure at $560°C$ to $600°C$ for 3 to 5 minutes. Growth mechanism of the graphene on Ni surface is not very straight forward. The growth mode depends mostly on the growth temperature and pressure. The temperature window for growing graphene on nickel by the surface growth is small. As carbon atoms form nickel carbide below 500c and could not form any graphene at high temperature, we chose temperature from $560°C$ to $620°C$ to grow graphene [64]. The STM images, shown in the Figure 25 (a),(b) are taken after graphene growth. From this image we can speculate that carbon atoms displace the nickel atoms from the nickel terraces, and thus form a hexagonal shape graphene. By analyzing line profile data (see Figure 25(c)), as there are almost no step height differences, we can also argue that the graphene is embedded into the first metal layer. The periodicity of the pattern is about 4 nm. As discussed earlier, the lattice constant of graphene and nickel (111) surface are closely matched, there should not be any moiré pattern unless the graphene sheet is rotated with respect to nickel surface.

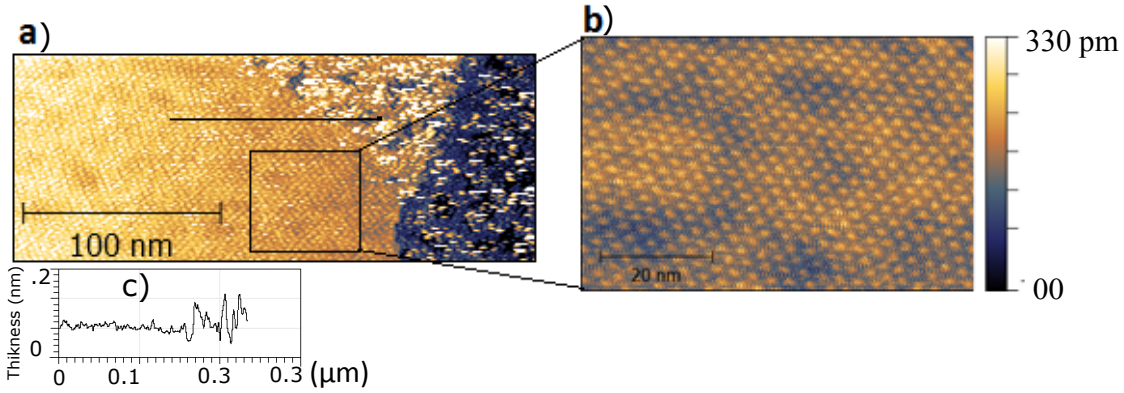

Figure 25: a) Graphene on nickel thin film. b) Graphene moiré pattern. c) The line profile on the first image.

The registry of first Ni atomic layer follows that of the underlying Ir lattice sites which induce strain in the Ni lattice. This strain decreases with the increasing of the atomic layer. If nickel thin film consists of few atomic layer, the topmost layer of the nickel film can be strained. Therefore the lattice constant of the nickel surface might be changed which leads to a superstructure (see the Figure 24(b)). As discussed in 2.4 section, moiré pattern leads strain in the G/h-BN interface. Thus, we can conclude that using nickel thin film is not feasible to grow G/h-BN interface.

In addition to graphene growth, we tried to synthesize h-BN on nickel thin film separately. To synthesize h-BN borazine ($B_3N_3H_6$) was used as a source material. The nickel thin film was exposed into borazine at 2.8×10^{-8} mbar pressure in around $800°C$ temperature for 5 to 10 minutes. But there are no any characteristic triangle of h-BN is seen in STM image. Therefore making a well defined heterostructure of graphene and h-BN is not possible in nickel thin film, and thus we prefer to have nickel single crystal on which the registry of superstructure can be followed by the 1×1 orientation.

4.2 Graphene and h-BN heterostructure growth on Ni(111)

As the structure of the graphene grown on nickel thin film is not well defined, we did not want to continue using it to make graphene and h-BN lateral heterostructures. As we wanted to have atomically well defined graphene and h-BN structure, Ni single crystal is good candidate for this purpose. As mentioned earlier, the lattice constant of Ni(111) is very closely matched to graphene and h-BN lattice constant, there should not be moiré pattern of graphene or BN. Ni(111) is also strongly interacted crystal facet for graphene and h-BN which allows these both materials to form (1×1) structures on Ni (111). To synthesis h-BN and graphene heterostucture, we grow h-BN before graphene growing as the growth temperature window for the h-BN is higher than for graphene. The growth temperature of the h-BN on Nickel veries between 700°C to 900°C, while graphene cannot sustain this high temperature due to the high carbon solubility in nickel. The h-BN has been obtained in a low pressure CVD system, by exposure of clean Ni(111) surface to the Borazine ($B_3N_3H_6$) gas at low 10^{-8} mbar pressure for 5 to 10 minutes. Thermal decomposition of borazine at a high temperature (> 700°C) on transition metal surfaces under vacuum conditions usually leads to a self-limiting growth, which forms monolayer h-BN [65]. As we want to have monolayer h-BN, the growth temperature was adjusted from 780C to 850C. The growth mode of h-BN on Ni(111) can be understood by analyzing Figure 26. Like graphene, the BN also displace nickel atoms from Ni (111) terraces and form highly symmetric triangular islands embedded into the first metal layer. By analysing line profile (see Figure26(c)) drawn across the BN triangle, having no step hight differences between BN and Nickel interface, we can speculate that BN displaces first atomic layer of nickel and form embedded BN. BN edges exhibit some roughness (see Figure 26(a) and (b)) when most of the other BN edges are sharp at the atomic level, and the length of the edges easily exceeds 150 nm. Most of the BN triangles are attached with edges of nickel terraces by one side, while the other sides are on the same terrace. We have also observed that the one angle of BN triangle (corner from the side, which is attached with a Ni step) is not symmetric. For this reason we also assume that the BN growth starts from the edges of the Ni terraces and continues onto terraces. In addition to this, there are some BN triangles

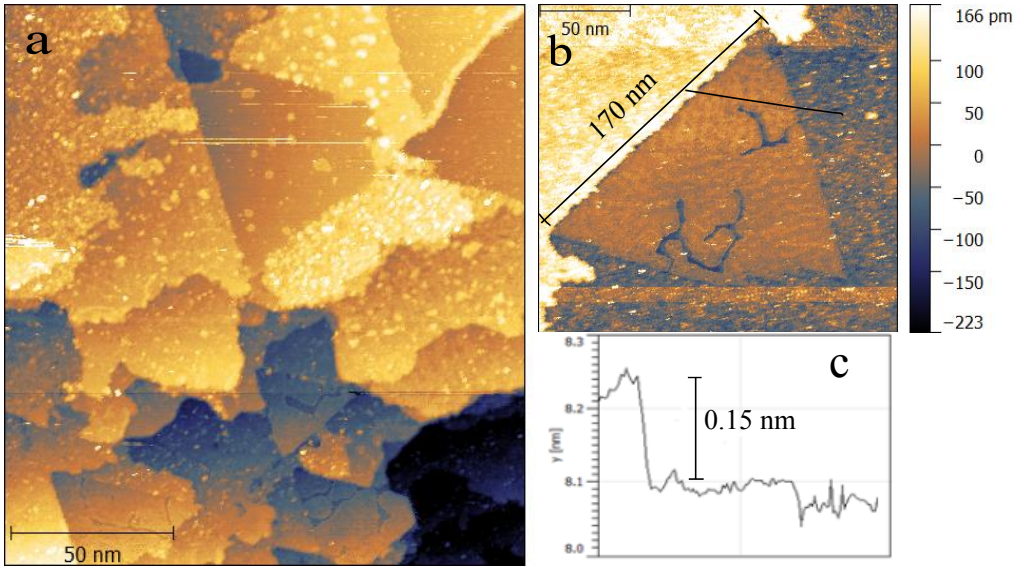

Figure 26: h-BN structure on nickel single crystal (a) Characteristics BN triangles. (b) A single BN triangle. (c) Line profile accros BN triangle.

which grows in the middle of the terraces. The length of the BN edges varies between 50 nm to 300 nm.

The edges of the BN triangles serve as seeds for the nucleation of the graphene on the Ni(111). Decomposition reaction of hydrocarbon occurs on bare nickel surface. So after BN synthesis, the growth of the graphene depends on the coverage of it. We optimized the amount of the borazine doses to get equal concentration of C, B, and N on the nickel surface. 30L exposure of the borazine and 60L for ethylene give very less carbon intensity (see Figure 27) in AES measurement compare to B and N. With the decreasing of the borazine dose, the carbon intensity increases in AES measurement. This observation proves that the nickel surface was almost covered by BN for 30L exposure and, for this reason no bare nickel surface left to act as catalyst in ethylene decomposition reaction. However we set 10L exposure of borazine with 60L for ethylene which give the equal concentration of the C, B, and N. In addition to this, there should be equal amount of coverage by graphene and BN so that transferred graphene and h-BN can be identified easily by Raman Spectroscopy. As it is said before, the exposure of borazine above 30 L reduces the amount of graphene coverage (see Figure27), we kept this value below this amount. Thus the Ni(111) containing BN is exposed to ethylene in 2×10^{-7} mbar pressure for 5 minutes (60L) at the growth temperature. By analysing AES data we can conclude that these parameters (10 L for borazine and 60 L for ethylene) give us optimum ratio of the graphene and h-BN coverage on Ni(111).

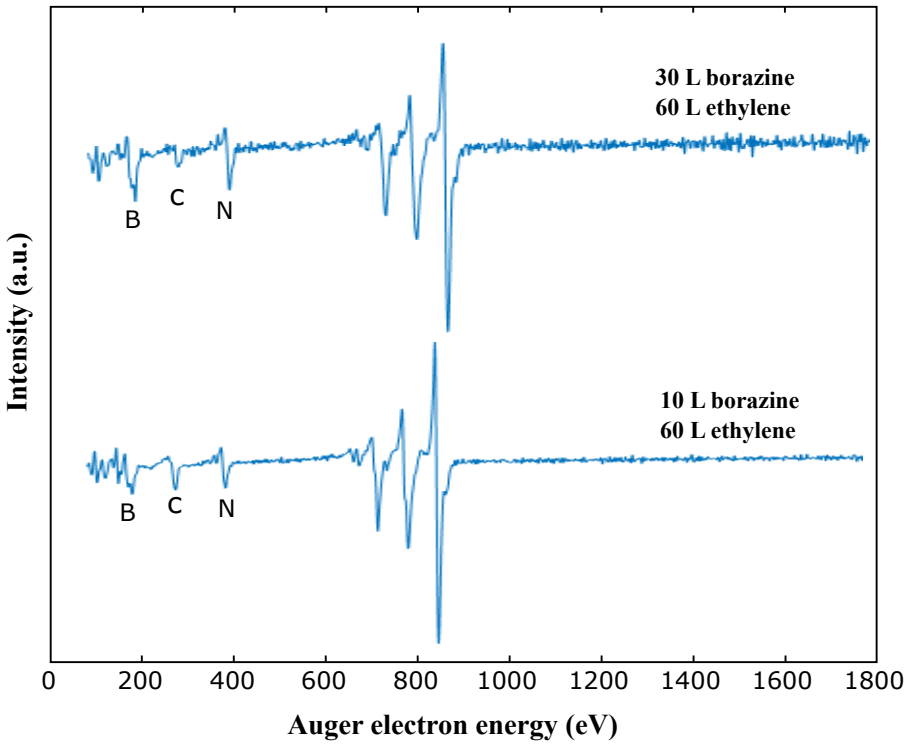

Figure 27: AES data of Gr-BN sample: The peak intensity ratio of carbon with respect to nickel for the first sample (30 L borazine) is less then the second sample(10 L borazine).

The deposition of graphene, grown by CVD at 600°C, does not effect the shape of the BN islands. It is clear that the edges of BN act as seed for the growth of graphene which are found attached to BN crystals, but never on bare surface. The nickel surface atoms are replaced by the carbon atoms at the edge of BN triangles and the graphene is formed in the same plane along BN seed. The shape of the graphene domain attached to BN triangle depends on the preparation conditions. For large partial pressure (above 10^{-7} mbar) of ethylene, the graphene starts to nucleate simultaneously at several places along BN edges. These graphene grains can be extended by decreasing the ethylene partial pressure shortly after nucleation. For this reason a jagged triangular graphene domain embedding the BN triangle are formed. An example of such BN triangle surrounded by graphene is shown in the Figure 30(a),(b). The STM images, as shown in the Figure 30(c), clearly shows the graphene and h-BN interface, and also proves that both graphene and BN are locked in the same plane. The interface is produced along ZZ direction of graphene and BN. As the BN triangles are stable during graphene growth, the total length of interfaces produced by this method is only limited by the size of BN seeds available.

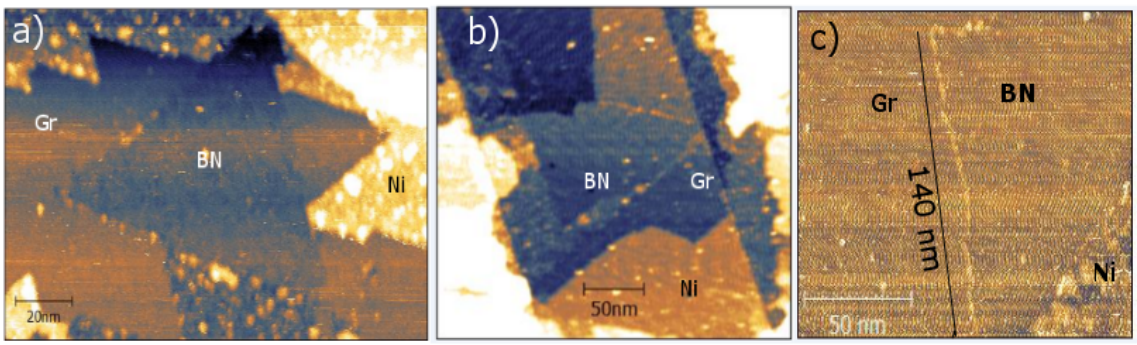

Figure 28: Gr-BN heterostructure. (a)and (b) A BN triangle encapsulated by graphene. (c) The interface between graphene and BN.

4.3 Graphene-BN heterostructure Transfer

After making a graphene-BN heterostructure, we need to transfer it onto an insulating substrate for further characterization and potential applications. The currently used etching-based transfer method is not suitable for the transfer of graphene-BN heterostructure grown on Ni(111). Ni(111) crystal is too expensive in compare to the Ni or Cu foils. In general, transferred graphene and h-BN contain metal contamination after etching. Recently, an electrochemical delamination method was reported to transfer graphene grown on Cu [12] and Pt [13] . We have used this electrochemical bubbling transfer technique, illustrated in the Figure 29, to transfer our heterostructure.

However, there are no reports on using the electrochemical bubbling process to transfer graphene-BN heterostructure so far. Therefore, to optimize the transfer process, firstly we have transferred the graphene grown on nickel foil onto a SiO_2 substrate. In this method, graphene is coated with polymethyl methacrylate (PMMA). This PMMA/graphene/Ni was dipped into an NaOH aqueous solution and used as cathode of an electrolysis cell with a constant current supply. On the cathode, a water reduction reaction takes place to produce H_2. This produced H_2 bubbles under the graphene, pushes the graphene supported PMMA film off from the substrate. On the other, if PMMA/graphene/Ni was used as an anode, the graphene might be oxidised due O_2 evolution. To avoid this unwanted oxidization, the sample was used as the cathode in the electrochemical cell.

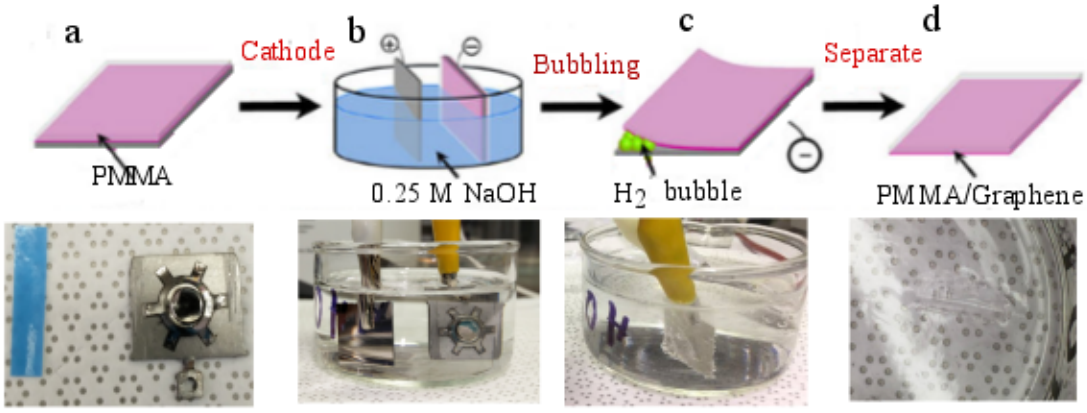

Figure 29: Ni single crystal with grown graphene-BN heterostructure covered by PMMA. (b) The PMMA/Gr-BN/Ni(111) is used as cathode in NaOH aqueous solution. (c) The PMMA/Gr-BN was gradually separated from the Ni(111) substrate driven by the H_2 bubbles produced at the cathode after applying a constant current. (d) The completely separated PMMA/Gr-BN layer floating on the NaOH solution.

We observed that the bubbling starts at the voltage 1.2 V. The more voltage is increased, the more bubbles are produced. We set the voltage to about 2.7 V for this experiment. The PMMA/graphene layer was partially detached from the Ni foil after 1 minute. The detachment of this layer depends on the concentration of both the PMMA and NaOH aqueous solution. To optimize the concentration and thickness of the polymer, we have used two different concentrations of PMMA (A3 and A9) in this experiment. We have also observed that higher concentration PMMA gives a stiffer polymer film than the lower concentration PMMA. For this reason the highly concentrated PMMA/graphene layer was detached from the foil in less than 30s. Again for the less concentrated PMMA it took longer time (5 to 20 minutes) to detach from the nickel surface.

Raman Spectroscopy and AFM have been used for further characterization of the transferred graphene. The quality of transferred graphene may depend on the concentration of the PMMA and the NaOH solution. From the Raman measurements, we have observed that the transferred graphene has large D band intensity near 1260 cm^{-1}. This means the graphene we have transferred, contains defects. The intensity of the G band is less than the 2D band which proves that we have grown a monolayer graphene on the nickel foil. AFM images shown in Figure 30(b),(d) are also taken to analyse the graphene film quality. We have noticed wrinkles on the graphene film created by the transfer process. From the optical images (shown in Figure 30(a)) we can also see that the graphene film was folded at some edges. In addition to this, some amount of polymer residue has also observed in both AFM and optical images. However, from Raman and AFM measurement we can say that graphene is transferred successfully by the bubbling transfer method .

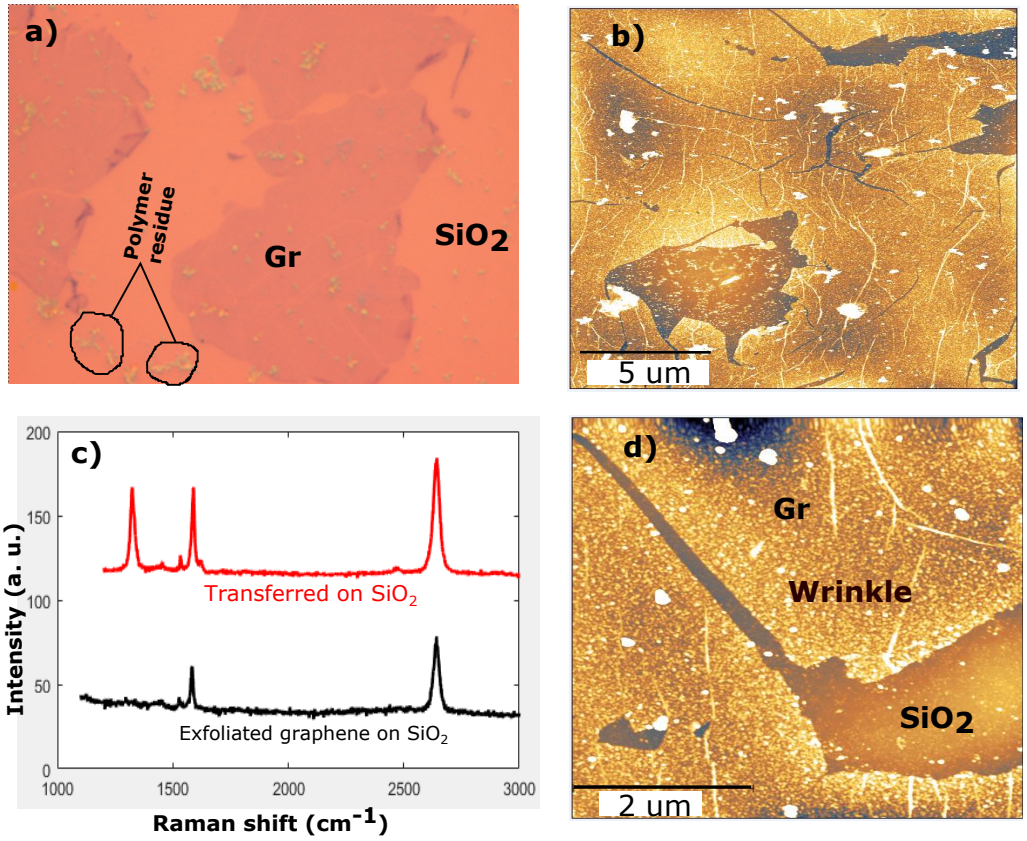

Figure 30: Transferred graphene films from Ni foil onto SiO_2/Si substrate. (a) Optical photograph of the transferred graphene on top of SiO_2/Si. Two black circles show the remaining polymer residue. (c) Raman spectroscopy of the graphene. (b), (d) AFM images of transferred graphene.

Although transfer of the graphene grown on nickel foil has been successfully demonstrated, Gr-BN heterostructure transfer into SiO_2/Si was the main target. The Gr-BN heterostructure has been synthesized on Ni(111). To transfer this heterostructure, the same procedure has been followed as for graphene transfer by electrochemical delamination method. But there was nothing found in Raman measurement after delamination process. In the case of Ni(111), the delamination time drastically decreases to half of the taken time for nickel foil. There might be several reasons for the failure of this transfer process. The highly reactive Ni(111) surface lead a strong interaction between Gr-BN heterostructure and nickel surface atoms. As the lattice constant of graphene, h-BN and Ni(111) are comparable to each other, the heterostructure forms a 1×1 registry with respect to Ni(111) surface, and thus the heterostructure attaches more strongly compare to the other metals. Another important possible reason might be that the gas evolution reaction takes place on graphene (and h-BN) instead of under them on the nickel surface. It is well-known that the h-BN on nickel becomes metallic because of charge transfer. In addition, the catalytic properties of graphene covered surfaces depend on the underlying substrate. If bubbles form on the graphene, the polymer film could delaminate leaving graphene on the Ni surface.

5 Conclusion and outlook

In this experiment, we have analysed the growth mechanism of graphene and h-BN on both Ni film and Ni(111), and we have demonstrated a method to synthesize Gr/h-BN heterostructures by a sequential deposition of BN and graphene.

We start by growing BN islands that are embedded in nickel terraces and terminated with zigzag-oriented edges. They serve as seeds for graphene growth. The size and shape of the graphene can be controlled by tuning the preparation conditions. The total length of the Gr-BN interface is only limited by the size of the BN seeds and we have successfully synthesised high quality G-BN interface of more than 160 nm length.

After the successful synthesis of the Gr/h-BN heterostructures, we tried to transfer them onto silicon wafer by electrochemical bubbling transfer method. While this method worked for transferring graphene grown on the Ni foil, it was unsuccessful for the Gr/h-BN heterostructures grown on the Ni(111). Possible reasons for this include too strong interaction between Gr/h-BN and Ni(111) or that the electrochemical gas evolution reaction would take place on top of Gr/h-BN film instead of the metal-heterostructure interface.

To make the transfer process successful few more things can be done in future. The transfer process of BN grown on Ni (111) is not well established. Therefore, we should check whether BN/Ni(111) can be transferred by using electrochemical bubbling transfer method. A second issue we need to address is the strong interaction between Gr/BN heterostructure and the Ni(111) substrate. This can probably be reduced by intercalating the heterostructure with different elements such as Br. The intercalation is an established procedure, and bromine intercalation has been demonstrated to enable the transfer of epitaxial graphene grown on Ir(111). Once intercalated, the heterostructure can be easily transferred by electrochemical transfer process. Combining the transfer techniques with our synthesis method should enable the manufacture of Gr/h-BN heterostructures well-defined interfaces and their transfer onto insulating substrates for transport measurements.

References

[1] A. K. Geim and I. V. Grigorieva, "Van der waals heterostructures," *Nature*, vol. 499, no. 7459, pp. 419–425, 2013.

[2] L. Britnell, R. Gorbachev, R. Jalil, B. Belle, F. Schedin, A. Mishchenko, T. Georgiou, M. Katsnelson, L. Eaves, S. Morozov *et al.*, "Field-effect tunneling transistor based on vertical graphene heterostructures," *Science*, vol. 335, no. 6071, pp. 947–950, 2012.

[3] Z. Liu, L. Ma, G. Shi, W. Zhou, Y. Gong, S. Lei, X. Yang, J. Zhang, J. Yu, K. P. Hackenberg *et al.*, "In-plane heterostructures of graphene and hexagonal boron nitride with controlled domain sizes," *Nature Nanotechnology*, vol. 8, no. 2, pp. 119–124, 2013.

[4] P. Sutter, Y. Huang, and E. Sutter, "Nanoscale integration of two-dimensional materials by lateral heteroepitaxy," *Nano Letters*, vol. 14, no. 8, pp. 4846–4851, 2014.

[5] Y.-W. Son, M. L. Cohen, and S. G. Louie, "Half-metallic graphene nanoribbons," *Nature*, vol. 444, no. 7117, pp. 347–349, 2006.

[6] D. Robert, K. Shawulienu, F. Schulz, A. Harju and P. Liljeroth, "Synthesis of extended atomically perfect zigzag graphene - boron nitride interfaces," *Scientific Reports*, vol. 5:16741, 2015.

[7] M. Liu, Y. Li, P. Chen, J. Sun, D. Ma, Q. Li, T. Gao, Y. Gao, Z. Cheng, X. Qiu *et al.*, "Quasi-freestanding monolayer heterostructure of graphene and hexagonal boron nitride on ir (111) with a zigzag boundary," *Nano Letters*, vol. 14, no. 11, pp. 6342–6347, 2014.

[8] R. Drost, A. Uppstu, F. Schulz, S. K. Hamalainen, M. Ervasti, A. Harju, and P. Liljeroth, "Electronic states at the graphene–hexagonal boron nitride zigzag interface," *Nano Letters*, vol. 14, no. 9, pp. 5128–5132, 2014.

[9] Y. Gao, Y. Zhang, P. Chen, Y. Li, M. Liu, T. Gao, D. Ma, Y. Chen, Z. Cheng, X. Qiu *et al.*, "Toward single-layer uniform hexagonal boron nitride–graphene patchworks with zigzag linking edges," *Nano Letters*, vol. 13, no. 7, pp. 3439–3443, 2013.

[10] J. Lu, L. C. Gomes, R. W. Nunes, A. Castro Neto, and K. P. Loh, "Lattice relaxation at the interface of two-dimensional crystals: Graphene and hexagonal boron-nitride," *Nano Letters*, vol. 14, no. 9, pp. 5133–5139, 2014.

[11] L. Liu, J. Park, D. A. Siegel, K. F. McCarty, K. W. Clark, W. Deng, L. Basile, J. C. Idrobo, A.-P. Li, and G. Gu, "Heteroepitaxial growth of two-dimensional hexagonal boron nitride templated by graphene edges," *Science*, vol. 343, no. 6167, pp. 163–167, 2014.

[12] Y. Wang, Y. Zheng, X. Xu, E. Dubuisson, Q. Bao, J. Lu, and K. P. Loh, "Electrochemical delamination of cvd-grown graphene film: toward the recyclable use of copper catalyst," *ACS Nano*, vol. 5, no. 12, pp. 9927–9933, 2011.

[13] L. Gao, W. Ren, H. Xu, L. Jin, Z. Wang, T. Ma, L.-P. Ma, Z. Zhang, Q. Fu, L.-M. Peng *et al.*, "Repeated growth and bubbling transfer of graphene with millimetre-size single-crystal grains using platinum," *Nature communications*, vol. 3, p. 699, 2012.

[14] A. K. Geim and K. S. Novoselov, "The rise of graphene," *Nature Materials*, vol. 6, no. 3, pp. 183–191, 2007.

[15] R. Drost, "Synthesis and electronic Properties of atomically well-defined Graphene Nanostructure," Ph.D. dissertation, Aalto University School of Science, 2016.

[16] N. M. R. P. K. S. N. A. H. Castro Neto, F. Guinea and A. K. Geim, "The electronic properties of graphene," *Reviews of Modern Physics*, vol. 81, pp. 109–162, 2009.

[17] K. S. Novoselov, A. K. Geim, S. V. Morozov, D. Jiang, Y. Zhang, S. V. Dubonos, I. V. Grigorieva, and A. A. Firsov, "Electric field effect in atomically thin carbon films," *science*, vol. 306, no. 5696, pp. 666–669, 2004.

[18] O. V. Yazyev and Y. P. Chen, "Polycrystalline graphene and other two-dimensional materials," *Nature Nanotechnology*, vol. 9, no. 10, pp. 755–767, 2014.

[19] D. Golberg, Y. Bando, C. Tang, and C. Zhi, "Boron nitride nanotubes," *Advanced Materials*, vol. 19, no. 18, pp. 2413–2432, 2007.

[20] L. Song, L. Ci, H. Lu, P. B. Sorokin, C. Jin, J. Ni, A. G. Kvashnin, D. G. Kvashnin, J. Lou, B. I. Yakobson *et al.*, "Large scale growth and characterization of atomic hexagonal boron nitride layers," *Nano Letters*, vol. 10, no. 8, pp. 3209–3215, 2010.

[21] Y. Shi, C. Hamsen, X. Jia, K. K. Kim, A. Reina, M. Hofmann, A. L. Hsu, K. Zhang, H. Li, Z.-Y. Juang *et al.*, "Synthesis of few-layer hexagonal boron nitride thin film by chemical vapor deposition," *Nano Letters*, vol. 10, no. 10, pp. 4134–4139, 2010.

[22] Z. Liu, Y. Gong, W. Zhou, L. Ma, J. Yu, J. C. Idrobo, J. Jung, A. H. MacDonald, R. Vajtai, J. Lou *et al.*, "Ultrathin high-temperature oxidation-resistant coatings of hexagonal boron nitride," *Nature communications*, vol. 4, 2013.

[23] A. Ismach, H. Chou, D. A. Ferrer, Y. Wu, S. McDonnell, H. C. Floresca, A. Covacevich, C. Pope, R. Piner, M. J. Kim *et al.*, "Toward the controlled synthesis of hexagonal boron nitride films," *ACS Nano*, vol. 6, no. 7, pp. 6378–6385, 2012.

[24] K. K. Kim, A. Hsu, X. Jia, S. M. Kim, Y. Shi, M. Hofmann, D. Nezich, J. F. Rodriguez-Nieva, M. Dresselhaus, T. Palacios *et al.*, "Synthesis of monolayer hexagonal boron nitride on cu foil using chemical vapor deposition," *Nano Letters*, vol. 12, no. 1, pp. 161–166, 2011.

[25] S. Chatterjee, Z. Luo, M. Acerce, D. M. Yates, A. C. Johnson, and L. G. Sneddon, "Chemical vapor deposition of boron nitride nanosheets on metallic substrates via decaborane/ammonia reactions," *Chemistry of materials*, vol. 23, no. 20, pp. 4414–4416, 2011.

[26] G. Kim, A.-R. Jang, H. Y. Jeong, Z. Lee, D. J. Kang, and H. S. Shin, "Growth of high-crystalline, single-layer hexagonal boron nitride on recyclable platinum foil," *Nano Letters*, vol. 13, no. 4, pp. 1834–1839, 2013.

[27] Y. Liu, S. Bhowmick, and B. I. Yakobson, "Bn white graphene with "colorful" edges: The energies and morphology," *Nano Letters*, vol. 11, no. 8, pp. 3113–3116, 2011.

[28] R. Y. Tay, M. H. Griep, G. Mallick, S. H. Tsang, R. S. Singh, T. Tumlin, E. H. T. Teo, and S. P. Karna, "Growth of large single-crystalline two-dimensional boron nitride hexagons on electropolished copper," *Nano Letters*, vol. 14, no. 2, pp. 839–846, 2014.

[29] A. Nagashima, N. Tejima, Y. Gamou, T. Kawai, and C. Oshima, "Electronic states of monolayer hexagonal boron nitride formed on the metal surfaces," *Surface science*, vol. 357, pp. 307–311, 1996.

[30] W. Auwärter, H. U. Suter, H. Sachdev, and T. Greber, "Synthesis of one monolayer of hexagonal boron nitride on ni (111) from b-trichloroborazine (clbnh) 3," *Chemistry of materials*, vol. 16, no. 2, pp. 343–345, 2004.

[31] K. Hermann, "Periodic overlayers and moiré patterns: theoretical studies of geometric properties," *Journal of Physics: Condensed Matter*, vol. 24, no. 31, p. 314210, 2012.

[32] R. Zhao, J. Wang, M. Yang, Z. Liu, and Z. Liu, "Bn-embedded graphene with a ubiquitous gap opening," *The Journal of Physical Chemistry C*, vol. 116, no. 39, pp. 21 098–21 103, 2012.

[33] J. Li and V. B. Shenoy, "Graphene quantum dots embedded in hexagonal boron nitride sheets," *Applied Physics Letters*, vol. 98, no. 1, p. 013105, 2011.

[34] A. Ramasubramaniam and D. Naveh, "Carrier-induced antiferromagnet of graphene islands embedded in hexagonal boron nitride," *Physical Review B*, vol. 84, no. 7, p. 075405, 2011.

[35] J.-W. Jiang, J.-S. Wang, and B.-S. Wang, "Minimum thermal conductance in graphene and boron nitride superlattice," *Applied Physics Letters*, vol. 99, no. 4, p. 043109, 2011.

[36] S. Jung, M. Park, J. Park, T.-Y. Jeong, H.-J. Kim, K. Watanabe, T. Taniguchi, D. H. Ha, C. Hwang, and Y.-S. Kim, "Vibrational properties of h-bn and h-bn-graphene heterostructures probed by inelastic electron tunneling spectroscopy," *Scientific reports*, vol. 5, 2015.

[37] L. Ci, L. Song, C. Jin, D. Jariwala, D. Wu, Y. Li, A. Srivastava, Z. Wang, K. Storr, L. Balicas *et al.*, "Atomic layers of hybridized boron nitride and graphene domains," *Nature materials*, vol. 9, no. 5, pp. 430–435, 2010.

[38] J. Coraux, M. Engler, C. Busse, D. Wall, N. Buckanie, F.-J. M. Zu Heringdorf, R. Van Gastel, B. Poelsema, T. Michely *et al.*, "Growth of graphene on ir (111)," *New Journal of Physics*, vol. 11, no. 2, p. 023006, 2009.

[39] P. Sutter, R. Cortes, J. Lahiri, and E. Sutter, "Interface formation in monolayer graphene-boron nitride heterostructures," *Nano Letters*, vol. 12, no. 9, pp. 4869–4874, 2012.

[40] Sutter, P and Cortes, R and Lahiri, J and Sutter, E, "Interface formation in monolayer graphene-boron nitride heterostructures," *Nano Letters*, vol. 12, no. 9, pp. 4869–4874, 2012.

[41] J. D. Caldwell, T. J. Anderson, J. C. Culbertson, G. G. Jernigan, K. D. Hobart, F. J. Kub, M. J. Tadjer, J. L. Tedesco, J. K. Hite, M. A. Mastro *et al.*, "Technique for the dry transfer of epitaxial graphene onto arbitrary substrates," *ACS Nano*, vol. 4, no. 2, pp. 1108–1114, 2010.

[42] Nano Letters Y. Lee, S. Bae, H. Jang, S. Jang, S.-E. Zhu, S. H. Sim, Y. I. Song, B. H. Hong, and J.-H. Ahn, "Wafer-scale synthesis and transfer of graphene films," *Nano Letters*, vol. 10, no. 2, pp. 490–493, 2010.

[43] M. Ishigami, J. Chen, W. Cullen, M. Fuhrer, and E. Williams, "Atomic structure of graphene on sio2," , vol. 7, no. 6, pp. 1643–1648, 2007.

[44] E. H. Lock, M. Baraket, M. Laskoski, S. P. Mulvaney, W. K. Lee, P. E. Sheehan, D. R. Hines, J. T. Robinson, J. Tosado, M. S. Fuhrer *et al.*, "High-quality uniform dry transfer of graphene to polymers," *Nano Letters*, vol. 12, no. 1, pp. 102–107, 2011.

[45] H. H. Kim, Y. Chung, E. Lee, S. K. Lee, and K. Cho, "Water-free transfer method for cvd-grown graphene and its application to flexible air-stable graphene transistors," *Advanced Materials*, vol. 26, no. 20, pp. 3213–3217, 2014.

[46] J. Kang, D. Shin, S. Bae, and B. H. Hong, "Graphene transfer: key for applications," *Nanoscale*, vol. 4, no. 18, pp. 5527–5537, 2012.

[47] Z. Cheng, Q. Zhou, C. Wang, Q. Li, C. Wang, and Y. Fang, "Toward intrinsic graphene surfaces: a systematic study on thermal annealing and wet-chemical treatment of sio2-supported graphene devices," *Nano Letters*, vol. 11, no. 2, pp. 767–771, 2011.

[48] Y.-C. Lin, C. Jin, J.-C. Lee, S.-F. Jen, K. Suenaga, and P.-W. Chiu, "Clean transfer of graphene for isolation and suspension," *ACS Nano*, vol. 5, no. 3, pp. 2362–2368, 2011.

[49] A. K. Geim and P. Kim, "Carbon wondeland," *Scientific American*, vol. 298, pp. 90 – 97, 2008.

[50] M. Batzill, "The surface science of graphene: Metal interfaces, {CVD} synthesis, nanoribbons, chemical modifications, and defects," *Surface Science Reports*, vol. 67, no. 3 "4, pp. 83 – 115, 2012.

[51] T. M. J. Lahiri and M. Batzill, "Graphene growth on ni (111) by transformation of a surface carbide," *Nano Letters*, vol. 2, p. 518–522, 2010.

[52] D. S. M. Olle, G. Ceballos and P. Gambardella, "Yield and shape selection of graphene nanoislands grown on ni(111)," *Nano Letters*, vol. 12, p. 4431–4436, 2012.

[53] P. S. R. Addou, A. Dahal and M. Batzill, "Monolayer graphene growth on ni (111) by low temperature chemical vapor deposition," *Applied Physics Letters*, vol. 100,, p. 021601, 2012.

[54] Patera, Laerte L and Africh, Cristina and Weatherup, Robert and Comelli, Giovanni and Hofmann, Stephan and others "In situ observations of the atomistic mechanisms of ni catalyzed low temperature graphene growth," *ACS Nano*, vol. 7,no. 9, p. 7901–7912, 2013.

[55] J. F. Watts and J. Wolstenholme, "An introduction to surface analysis by xps and aes," *John Wiley Sons*, 2003.

[56] P. Holloway, "Thickness determination of ultrathin films by auger electron spectroscopy," *Journal of Vacuum Science & Technology*, vol. 12, no. 6, pp. 1418–1422, 1975.

[57] I. G. John C. Vickerman, "Surface analysis: The principal techniques, 2nd edition," *Wiley*, 2009.

[58] P. Hofmann, *Surface Physics: An Introduction*, 2013.

[59] H. R. G. Binning, *Scanning Tunneling Microscopy*, 1986, vol. 30(4).

[60] C. Bai, *Scanning Tunneling Microscopy and its Application*, 2000.

[61] S. Hamalainen, "Modication of the electronic structure of graphene by quantum connement and molecular self-assembly," *PhD, Dissertation*, 2014.

[62] M. Lazzeri, C. Attaccalite, L. Wirtz, and F. Mauri, "Impact of the electron-electron correlation on phonon dispersion: Failure of lda and gga dft functionals in graphene and graphite," *Phys. Rev. B*, vol. 78, p. 081406, Aug 2008.

[63] L. Malard, M. Pimenta, G. Dresselhaus, and M. Dresselhaus, "Raman spectroscopy in graphene," *Physics Reports*, vol. 473, no. 5"6, pp. 51 – 87, 2009.

[64] R. Addou, A. Dahal, P. Sutter, and M. Batzill, "Monolayer graphene growth on ni (111) by low temperature chemical vapor deposition," *Applied Physics Letters*, vol. 100, no. 2, p. 021601, 2012.

[65] A. Preobrajenski, A. Vinogradov, and N. Mayrtensson, "Monolayer of h-bn chemisorbed on cu(1 1 1) and ni(1 1 1): The role of the transition metal 3d states," *Surface Science*, vol. 582, pp. 21 – 30, 2005.